# Oscillator stabilization through feedback with slow-wave structures

Mabel Pontón, *Member, IEEE*, Franco Ramírez, *Senior Member, IEEE*, Amparo Herrera, and Almudena Suárez, *Fellow, IEEE*

***Abstract*—This work presents a new formulation to predict the steady state, stability and phase-noise properties of oscillator circuits including either a self-injection network or a two-port feedback network for phase-noise reduction. The additional network contains a slow-wave structure that stabilizes the oscillation signal. Its long delay inherently gives rise to multivalued solutions in some parameter intervals, which should be avoided for a reliable operation. Under a two-port feedback network, the circuit is formulated extracting two outer-tier admittance functions, which depend on the node-voltage amplitudes, phase shift between the two nodes and excitation frequency. Then, the effect of the slow-wave structure is predicted through an analytical formulation of the augmented oscillator, which depends on the numerical oscillator model and the structure admittance matrix. The solution curves are obtained in a straightforward manner by tracing a zero-error contour in the plane defined by the analysis parameter and the oscillation frequency. The impact of the slow-wave structure on the oscillator stability and noise properties is analyzed through a perturbation method, applied to the augmented oscillator. The phase-noise dependence on the group delay is investigated calculating the modulation of the oscillation carrier. The various analysis and design methods have been applied to an oscillator at 2.73 GHz, which has been manufactured and measured, obtaining phase-noise reductions of 13 dB, under a one-port load network, and 18 dB, under a feedback network.**

***Index Terms*—Oscillator, phase-noise, slow-wave structure, stability.**

## I. Introduction

Phase noise is an undesired characteristic of oscillator circuits, which degrades their spectral purity and can give rise to demodulation errors [1]-[3]. The possibility to reduce the phase noise of an existing oscillator with the aid of long-delay lines, through self-injection locking or using frequency discriminators has been demonstrated in several previous works [4]-[10]. However, this is generally inconvenient [4]-[5], since the overall system becomes bulky due to the long physical lengths required to achieve a significant phase-noise improvement. As shown in [11], the problem can be circumvented with slow-wave structures [12]-[14] implemented on microstrip line. Actually, oscillators based on slow-wave resonators with excellent performance have been demonstrated in the literature [15]-[16]. Taking a different approach, the recent work [11] uses the slow-wave structure as an external network, in a manner similar to what is done in [4]-[10] with long cables and delay lines. As in those previous works, the aim is to increase the oscillator quality factor, which is enabled by the high group delay of the slow-wave structure. The phase-noise reduction is achieved through a suitable synthesis of the slow-wave structure only, without having to redesign the oscillator circuit.

The structure must be optimized to maximize the phase-noise reduction, while ensuring a stable operation of the augmented oscillator. Note that instability problems resulting from the use of long delay lines and high quality-factor resonators have been reported in previous works [4], [17]. For this optimization, a new methodology is presented here, which departs from accurate numerical models of both the oscillator and the slow-wave structure. Their interaction is described through an analytical formulation of the augmented oscillator, which enables a realistic and insightful prediction of the effect of the structure.

In comparison with the previous work [11], two different ways to introduce the slow-wave structure are considered: as a one-port configuration, connected to the oscillator output, and as an external two-port feedback network. The numerical model that describes the oscillator can be obtained through harmonic balance (HB) simulations [18]-[20] or through experimental measurements [21]. When using HB, the standalone oscillator is modeled with outer-tier admittance functions, extracted with the aid of auxiliary generators (AG) [18]-[20]. The two-port feedback network requires a two-port oscillator model, derived here for the first time. The model is extracted through the simultaneous connection of two AGs at the two circuit nodes between which the two-port feedback network is introduced. In turn, this feedback network is described with its frequency-dependent 2×2 admittance matrix. Note that the strong frequency variation of long-delay elements inherently gives rise to multi-valued solution curves under moderate attenuation. [11]. These curves cannot be obtained without complementary continuation techniques [22]-[23], which are not available by default in commercial HB software. Instead, the new formulation is able to provide

Manuscript received May 3, 2019. This paper is an expanded version from the IEEE MTT-S International Microwave Symposium (IMS 2019), Boston, MA, USA, June 2-7, 2019. This work was supported by the Spanish Ministry of Economy ans Competitiveness through the European Regional Development Fund(ERDf)/ Fondo Europeo de Desarooloo Regional (FEDER) and under Project TEC2017-88242-C3-(1/2)-R.

M. Pontón, F. Ramírez, A. Herrera and A. Suárez are with the Departamento de Ingeniería de Comunicaciones, Universidad de Cantabria, Santander, 39005, Spain (e-mail: mabel.ponton@unican.es; ramirezf@unican.es; herreraa@unican.es; suareza@unican.es).

the multi-valued curves in a straight-forward manner and with a high accuracy. The main advantage of the new method is its generality of application to oscillators with arbitrary topologies, using any kind of slow-wave structure. This is because it relies on a numerical admittance description of the structure that can even be obtained through an electromagnetic simulation.

Two different slow-wave structures will be considered. One has a unit cell made up of an open-ended stub and a Schiffman section [14], [24]. The other one is based on a simple distributed implementation of the inductors and capacitors in a discrete transmission line. The oscillator stability and noise are analyzed through a perturbation method, here applied, for the first time, to a formulation relying on two outer-tier admittance functions. In the presence of a two-port feedback network, the phase noise is predicted in two different manners. In the first one, the phase perturbations at the two analysis nodes are considered as system variables. In the second one, a direct calculation of the perturbed frequency is performed, as in the carrier-modulation approach [25]. Though the first formulation is more accurate, the second one enables a better insight into the mechanism for phase-noise reduction, which will be analytically related to the group delay of the slow-wave structure. The analysis and synthesis methods have been applied to an oscillator at 2.73 GHz, which has been manufactured and measured. The accuracy is validated through comparisons with experimental measurements and circuit-level simulations (when HB convergence is achieved).

The paper is organized as follows. Section II presents the analysis of the oscillator loaded with a one-port network. It comprises three subsections devoted to the calculation of the steady-state solutions, including the new zero-error contour, the stability analysis and the phase-noise analysis. Section III addresses the case of two-port feedback network, also considering the steady-state solutions, the stability analysis and the phase-noise analysis.

## II. Oscillator Loaded with a One-Port Network Containing a Slow-Wave Structure

This section analyzes the effect of a slow-wave structure, connected to the output port of the oscillator circuit (Fig. 1).

### A. Steady-state solutions

Let a free-running oscillator circuit be considered. The total admittance function must be equal to zero at all the circuit nodes [26]-[32] and, in particular, at the output node where the network containing the slow-wave structure will be connected. At this output node, the circuit fulfils the following steady-state oscillation condition, at the fundamental frequency:

$$Y_T(V_o,\omega_o) = Y(V_o,\omega_o) + Y_o = 0 \qquad (1)$$

where $V_o$ is the first-harmonic amplitude, $\omega_o$, the oscillation frequency and $Y_o = 0.02\ \Omega^{-1}$, the standard termination load. The solution $(V_o,\omega_o)$ of the standalone oscillator can be obtained using an auxiliary generator (AG) [26]-[27]. This is an artificial generator, in series with an ideal bandpass filter, connected in parallel at the analysis node (Fig. 1). It operates at the oscillation frequency $\omega_{AG} = \omega_o$, with the amplitude $A_{AG} = A_o$. Both of them are unknowns that must be calculated during the solution process. They must provide a zero value of the AG current-to-voltage ratio [26]-[27] $Y_{AG}(A_{AG}, \omega_{AG}) = 0$, which avoids the trivial solution with zero amplitude ($A_{AG} = 0$).

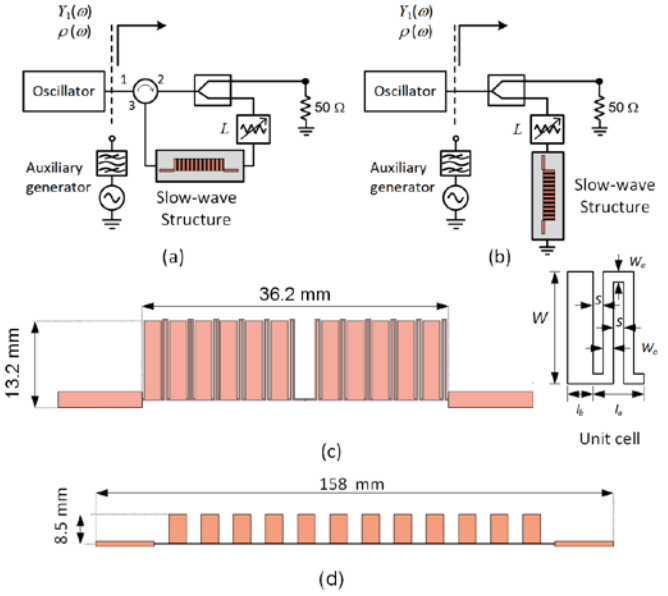


Fig. 1. Oscillator loaded with a one-port network containing a slow-wave structure. (a) Configuration based on a circulator. (b) Simpler configuration based on a slow-wave structure terminated in a short circuit. (c) Slow-wave structure based on a unit cell made up of a Schiffman section and an open-ended stub. (d) Slow-wave structure based on a simple distributed implementation of the inductors and capacitors in a discrete transmission line.

Next, a one-port network containing the slow-wave structure and exhibiting the input admittance $Y_1(\omega)$ will be considered (Fig. 1), replacing the termination load $Y_o$. In the presence of this one-port network, the total admittance function is:

$$Y_T(V,\omega) + \left[Y_1(\omega) - Y_o\right] = Y_T(V,\omega) + Y_L(\omega) = 0 \qquad (2)$$

where $Y_L(\omega)$ is the additional load admittance due to the introduction of the one-port network. This may contain a circulator [Fig. 1(a)] such that the oscillator output is connected to Port 1 and the slow-wave structure is connected between Port 2 and Port 3. This is the set-up proposed in [4]-[5], using long cables to obtain a high delay. Here, a simpler topology, shown in Fig. 1(b), is proposed, which avoids the need of a circulator and enables an increase of group delay, due to reflection effects. The additional load must not significantly alter the steady-state solution, so it includes an attenuator of $L$ dB. Thus, it should be possible to expand the admittance function $Y(V,\omega)$ in (1), in a first-order Taylor series about the free-running solution $(V_o,\omega_o)$ of the standalone oscillator:

$$\frac{\partial Y(V_o,\omega_o)}{\partial V}(V - V_o) + \frac{\partial Y(V_o,\omega_o)}{\partial \omega}(\omega - \omega_o) + Y_L(\omega) = 0 \qquad (3)$$

where $V$ and $\omega$ are the oscillation voltage amplitude and fundamental frequency, in the presence of the additional load, and higher order terms have been neglected. Note that the full frequency variation of $Y_L(\omega)$ is considered since, due to the

long delay, it will exhibit significant changes versus $\omega$. In simulation, the derivatives of the admittance function $Y(V,\omega)$ are extracted from a HB analysis of the standalone oscillator, using an AG. The AG is connected in parallel at the same node where the one-port network is introduced, and the derivatives are calculated applying finite differences to the AG amplitude and frequency, as described in [18]-[19]. The derivatives are obtained using any suitable number (NH) of harmonic terms. In all the analyses performed in this work NH = 15 has been considered.

Splitting (3) into real and imaginary parts,

$$\begin{aligned}\frac{\partial Y_r}{\partial V}(V-V_o)+\frac{\partial Y_r}{\partial \omega}(\omega-\omega_o)+Y_L^r(\omega)=0\\ \frac{\partial Y_i}{\partial V}(V-V_o)+\frac{\partial Y_i}{\partial \omega}(\omega-\omega_o)+Y_L^i(\omega)=0\end{aligned} \tag{4}$$

where the subscripts and superscripts *r* and *i* indicate real and imaginary parts. Solving for $(\omega-\omega_o)$, one obtains:

$$\omega=\omega_o+\frac{\partial Y_r}{\partial V}\frac{Y_L^i(\omega)}{\det_o}-\frac{\partial Y_i}{\partial V}\frac{Y_L^r(\omega)}{\det_o} \tag{5}$$

where $\det_o$ is:

$$\det_o=\frac{\partial Y_r}{\partial V}\frac{\partial Y_i}{\partial \omega}-\frac{\partial Y_r}{\partial \omega}\frac{\partial Y_i}{\partial V} \tag{6}$$

To get some insight into the shape of the solution curves, one can express $Y_L(\omega)$ in terms of the reflection coefficient $\Gamma = \rho\exp(j\phi)$ associated with $Y_1(\omega)$.

$$\begin{aligned}Y_L(\omega)&=Y_o\frac{1-\Gamma(\omega)}{1+\Gamma(\omega)}-Y_o\cong\big(1-2\Gamma(\omega)\big)Y_o-Y_o\\ &=-2\rho(\omega)e^{j\phi(\omega)}Y_o\end{aligned} \tag{7}$$

where it has been taken into account that $\Gamma(\omega)$ must have a low magnitude. Due to the long delay, the real and imaginary parts of $Y_L(\omega)$ will vary nearly sinusoidally with $\omega$ [also affected by $\rho(\omega)$]. The solutions of (5) will correspond to the intersections of a straight line ($\omega$-$\omega_o$) and a nearly-sinusoidal function, which [for not too small $\rho(\omega)$] is susceptible to provide several distinct points for some $\phi(\omega)$.

To optimize the slow-wave structure, one should be able to predict the variation of the oscillation frequency $\omega$ versus any parameter $\eta$ of this structure. This can be done taking advantage of the capability of commercial circuit-simulation software to provide constant-value contours of a given scalar quantity. Using (5), a zero-error contour is defined:

$$E(\eta,\omega)=\omega-\omega_o-\frac{\partial Y_r}{\partial V}\frac{Y_L^i(\eta,\omega)}{\det_o}+\frac{\partial Y_i}{\partial V}\frac{Y_L^r(\eta,\omega)}{\det_o}=0 \tag{8}$$

Note that the coefficients $\frac{\partial Y_r}{\partial V}\frac{1}{\det_o}$ and $\frac{\partial Y_i}{\partial V}\frac{1}{\det_o}$ are constant values calculated only once, from the initial simulation of the standalone free-running oscillator [see flowchart of Fig. 2(a)]. To obtain the contour, only the linear slow-wave structure is simulated, since, due to the relatively high attenuation, $Y_L(\eta,\omega)$ has a small magnitude, so it will not affect the Taylor series expansion of the oscillator admittance. A double sweep in $\eta$ and $\omega$ is carried out to obtain the double entry function $Y_L(\eta,\omega)$. Then, the solution curve, in terms of $\omega$ versus $\eta$, agrees with the zero-value contour of $E(\eta,\omega)$. Fig. 2(b) shows how the contour equation $E(\eta,\omega)=0$ is introduced in the circuit-simulation software. Once $\omega$ is known, the increment in the oscillation amplitude $\Delta V = V - V_o$ is directly obtained by replacing $\omega$ in (3).

Fig. 3(a) and (b) present an oscillator at 2.73 GHz, based on the transistor ATF34143. The prototype has an input port between the terminal *T* and ground, where a connector is used to introduce the feedback network at a later stage. Fig. 3(c) presents the measured phase-noise spectrum with and without the connector at *T*, obtained with the R&S FSWP8 - Phase Noise Analyzer and VCO Tester. For the phase-noise reduction, a slow-wave structure based on a unit cell made up of a Schiffman section and an open-ended stub (SS-OS) [13], [24] has been used, which is shown in Fig. 1(c). The dimensions of this structure are 36.2 mm (length) x 13.2 mm (width). Additionally, a slow-wave structure based on a simple distributed implementation of the inductors and capacitors in a discrete transmission line [Fig. 1(d)] will be considered in some specific tests. Its dimensions are 158 mm (length) x 8.5 mm (width). Note that the first step in the optimization procedure is to achieve a high value of the group-delay of the slow-wave structure at the desired oscillation frequency, which in this case is $f_o$ = 2.73 GHz. Fig. 4(a) compares the measured group delay of the two configurations. The structure in Fig. 1(d) exhibits a high maximum but it is too close to the limit of the passband. The group delay of the SS-OS structure is lower, but maintains reasonably high values in a broader bandwidth about the intended oscillation frequency.

A relevant parameter of the slow-wave structure in Fig. 1(c) the transversal length *W*. In Fig. 5(a), the contour $E(W,\omega)=0$, obtained with the topology in Fig. 1(b), under the attenuation *L* = 6 dB, has been traced in the plane defined by the *W* and $\omega$. In a manner similar to the solutions obtained with the circulator [11], the curves are multi-valued in some *W* intervals. The frequency excursions are similar in the two cases. The frequency $\omega$ obtained from the numerical solution of (5) agrees with the one resulting from the contour $E(\eta,\omega)=0$ in (8), since the two equations are identical. However, (8) is solved through an error-minimization method and the contour is calculated through spline interpolation. The results of the analytical formulation have also been compared with those obtained through a demanding HB simulation of the whole oscillator system (including the slow-wave structure), with NH = 15. For this simulation, an auxiliary generator was used, since it was not possible to obtain convergence with the default oscillator analysis of the commercial HB software in wide intervals of the parameter *W*. Though the oscillator core is simple, when loaded with the slow-wave structure multi-valued regions arise in the solution curve, delimited by turning points, at which the Jacobian matrix is singular. Convergence problems arise in the HB system even before reaching these points, due to the ill-conditioning of the Jacobian matrix. This prevents the user from getting sufficient information on the form of variation of the solution curve. The auxiliary-generator technique is more

flexible, since it enables the optimization of three variables, including the parameter $\eta = W$, to fulfill the non-perturbation condition $Y_{AG} = 0$.

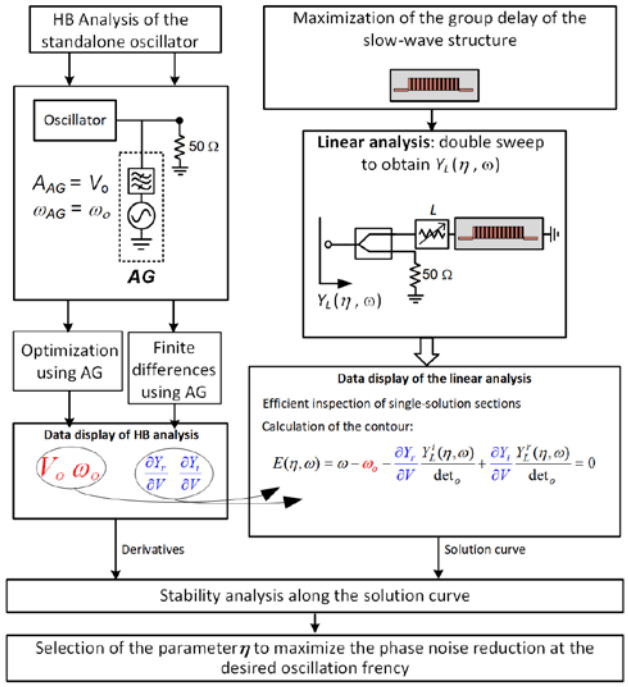


(a)

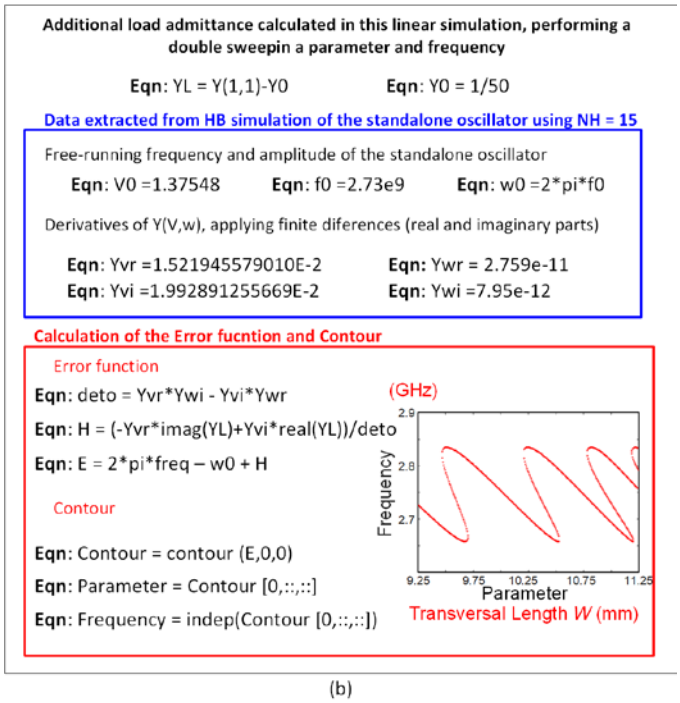


(b)

Fig. 2. Flowchart. (a) Steps of the analysis and design methodology, with emphasis on the calculation of the solution curves by tracing the contour $E(\eta,\omega) = 0$ . (b) Replica of the data display of the circuit-simulation software with contour-tracing capabilities. It shows how the contour equation $E(\eta,\omega) = 0$ is introduced.

The agreement with HB is very good, only degrading about the maximum frequency excursions, due to the limitations of the Taylor-series approximation. This good agreement is because the oscillator model based on $\frac{\partial Y}{\partial V}$ and $\frac{\partial Y}{\partial \omega}$ is extracted using 15 harmonic terms. Though expression (4) only accounts for the effect of the additional one-port network at the fundamental frequency, the inherent filtering of the slow-wave structure reduces the impact of higher harmonic terms. This can be seen in the experimental measurement of Fig. 4(b), where the magnitude of the scattering parameter $S_{21}$ of the two slow-wave structures considered, shown in Fig. 1(c) and Fig. 1(d), has been represented versus frequency. The second and third harmonic components are attenuated more than 30 dB in the two cases.

In the analysis of Fig. 5(b), the transversal length $W$ is kept constant, varying the attenuation $L$. The oscillation frequency $\omega$ has been represented versus $L$ for two values of the transversal length, marked in Fig. 3(a): $W_1$, providing an oscillation frequency equal to the free-running one, $f = f_o = 2.73$ GHz, and $W_2$, providing a higher frequency. Note that the goal will be to set the operation point at the frequency of the original free-running oscillator $\omega_o$, since, in general, frequency shifts are undesired. The solution curves have been obtained tracing the zero-error contour $E(L,\omega) = 0$ . The consistency between (a) and (b) can be noted. The multivalued sections arise when reducing the attenuation $L$. For $W_1$ the oscillation frequency keeps nearly constant at $\omega_o$ for all the $L$ values. For any other $W$, it tends to $\omega_o$ when increasing the attenuation. Note that the optimum set of parameters should be selected after examining the system stability and phase-noise properties, which are the object of the next two subsections.

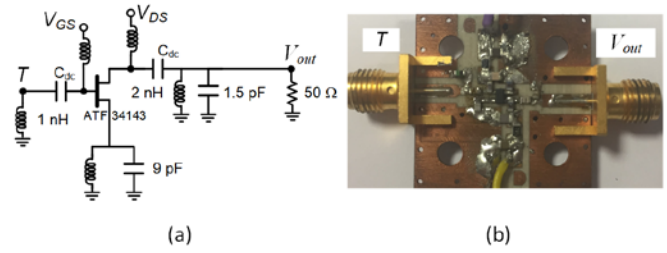


(a) (b)

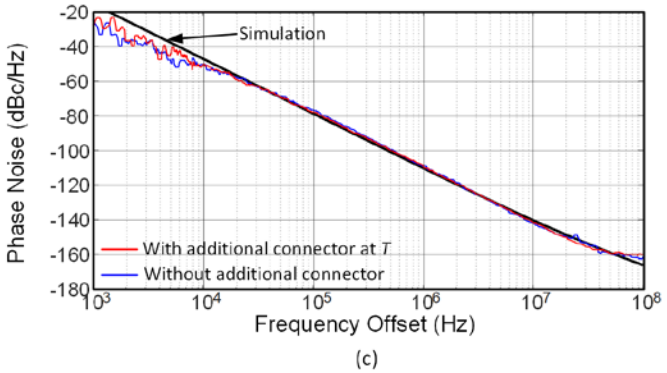


(c)

Fig. 3. Oscillator based on the PHEMT transistor ATF34143 operating at 2.73 GHz. (a) Schematic. (b) Photograph of the prototype built on Rogers 4003C. (c) Characterization of the phase noise of the standalone oscillator with the R&S FSWP8 analyzer. Comparison with the simulated phase-noise spectrum after fitting the equivalent nose current source $\langle |I_N^2| \rangle$ with $|I_w|^2 = 0.25\ 10^{-20}$ A$^2$/Hz and $k/f = 1.91\ 10^{-14}/f$ A$^2$/Hz.

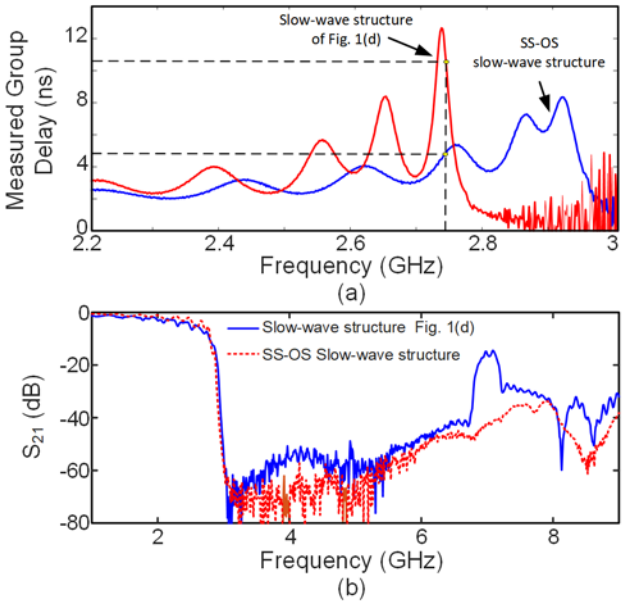


Fig. 4. Experimental characterization of the slow-wave structures in Fig. 1(c) and Fig. 1(d), with the respective dimensions 36.2 mm (length) x 13.2 mm (width) and 158 mm (length) x 8.5 mm (width). (a) Group delay, which should have a high value at the desired oscillation frequency (2.73 GHz). (b) Magnitude of the scattering parameter $S_{21}$ in the two cases.

For an experimental validation, the solution curves have also been traced versus a parameter than can be varied continuously. This is the drain bias voltage $V_{DS}$ of the oscillator circuit. Thus, the numerical oscillator model must depend on $V_{DS}$, so it will be given by $V_o(V_{DS})$, $\omega_o(V_{DS})$, $\partial Y(V_{DS})/\partial V$, $\partial Y(V_{DS})/\partial \omega$. This model is extracted by performing a sweep in $V_{DS}$ and calculating the steady-state solution of the standalone oscillator, plus the admittance-function derivatives (through finite differences) at each sweep step. The resulting arrays are read and introduced in the error equation (4).

Fig. 6(a) presents the simulated solution curves, in terms of $\omega$ versus $V_{DS}$, for $W_2$ = 11.08 mm and $L$ = 8 dB. There is a closed curve, existing from $V_{DS}$ = 2 V to $V_{DS}$ = 2.76 V, and an open curve at higher frequency values. This result is compared with the experimental trace, obtained using the mode for VCO characterization of the R&S FSWP8 analyzer. This experimental trace corresponds to the lower section of the closed curve. A jump occurs at $V_{DS}$ = 2.76 V, where the lower simulated curve exhibits a turning point (*TP*). At this point, the oscillation frequency undergoes a discontinuous increase, both in measurement and simulation. The latter predicts a jump to the upper solution curve. The shape of the curve is different in simulation and measurements, which is attributed to the limited accuracy of the models of the active and passive components in the oscillator core. We do not think that the accuracy problem comes from the formulation, since, as gathered from Fig. 5(a), it shows an excellent agreement with circuit-level simulations. However, for $W_2$ = 11.08 mm, the augmented oscillator is in a multi-valued interval of Fig. 5(a), corresponding to $V_{DS}$ = 2.7 V. In these conditions, small parameter variations will give rise to significant changes, due to the proximity of the turning points.

Fig. 6(b) presents the solution curve, in terms of $\omega$ versus $V_{DS}$, for $W_1$ = 10.1 mm and $L$ = 6 dB. Both the simulated and measured curves are single valued and exhibit an excellent agreement, better than the one obtained in Fig. 5(a). This is because $W_1$ = 10.1 mm corresponds to a single-valued interval of the solution curve in Fig. 5(a). The location of these single-valued sections exhibits little dependence on $V_{DS}$, since this bias voltage does not affect the drain-to-source capacitance, considered linear in the device model. Note that the goal of the analysis versus $V_{DS}$ is not to optimize the design of the oscillator system (as when using $W$ as a parameter) but to validate the prediction capabilities of the analysis method under the continuous variation of a parameter.

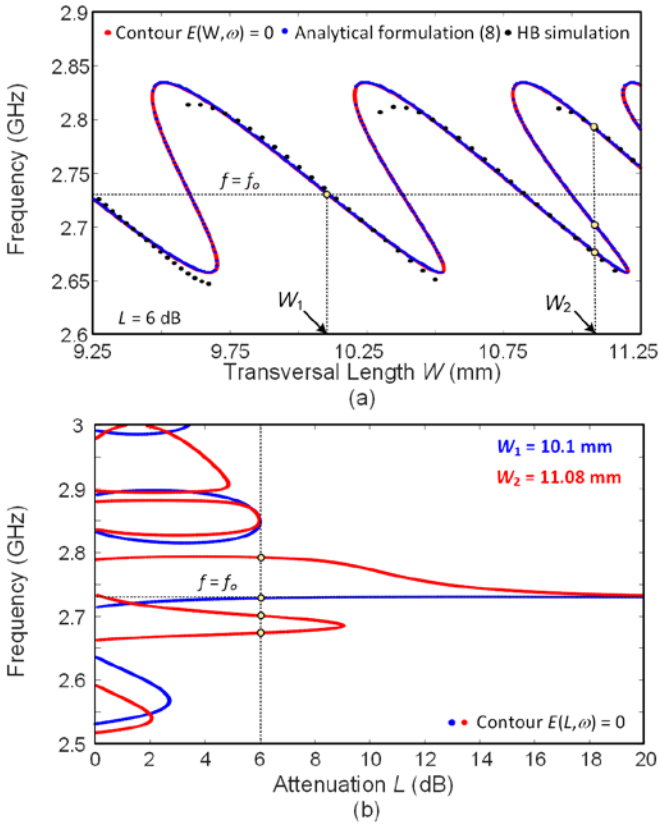


Fig. 5. Solution curves in terms of the oscillation frequency $\omega$. (a) When using the configuration in Fig. 1(b), under an attenuation $L$ = 6 dB. The zero-error contour $E(W,\omega)=0$ is validated through a comparison with a numerical solution of (4) and with circuit-level HB. (b) Solution curves versus the attenuation $L$ for two values of the transversal length in (a): $W_1$, providing an oscillation frequency equal to the free-running one, $f = f_o$ = 2.73 GHz, and $W_2$, providing a higher frequency.

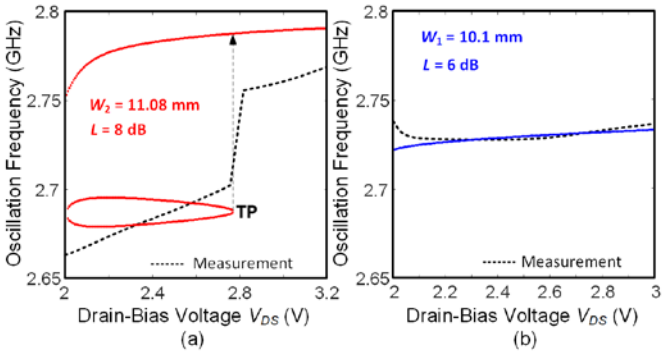


Fig. 6 Variation of the oscillation frequency $\omega$ versus the drain-bias voltage $V_{DS}$. Comparison with experimental measurements using the mode for VCO characterization of the R&S FSWP8 analyzer. (a) For $W_2$ = 11.08 mm and $L$ = 8 dB. (b) For $W_1$ = 10.1 mm and $L$ = 6 dB.

### *B. Stability analysis*

When applying a small perturbation to equation (3), the voltage amplitude and phase at the analysis node become $V+\delta V(t)$, $0+\delta\phi(t)$ and the frequency becomes $\omega - js$. Taking into account that the increment $s$ acts as a time differentiator [28]-[29], the perturbed system is:

$$\frac{\partial Y}{\partial V}\delta V+\left(\frac{\partial Y}{\partial \omega}+\frac{\partial Y_L(\omega)}{\partial \omega}\right)\left(-j\frac{\delta \dot{V}}{V_o}+\delta\dot{\phi}\right)=0 \tag{9}$$

Splitting the above equation into real and imaginary parts, and gathering the terms $[\delta\dot{V} \quad \delta\dot{\phi}]^T$ and $[\delta V \quad \delta\phi]^T$, one obtains:

$$\begin{bmatrix} \frac{1}{V_o}\left(\frac{\partial Y_i}{\partial\omega}+\frac{\partial Y_L{}^i(\omega)}{\partial\omega}\right) & \frac{\partial Y_r}{\partial\omega}+\frac{\partial Y_L{}^r(\omega)}{\partial\omega} \\ \frac{-1}{V_o}\left(\frac{\partial Y_r}{\partial\omega}+\frac{\partial Y_L{}^r(\omega)}{\partial\omega}\right) & \frac{\partial Y_i}{\partial\omega}+\frac{\partial Y_L{}^i(\omega)}{\partial\omega} \end{bmatrix}\begin{bmatrix}\delta\dot{V}\\ \delta\dot{\phi}\end{bmatrix}= -\begin{bmatrix} \frac{\partial Y_r}{\partial V} & 0 \\ \frac{\partial Y_i}{\partial V} & 0 \end{bmatrix}\begin{bmatrix}\delta V\\ \delta\phi\end{bmatrix} \tag{10}$$

System (10) can be rewritten in a compact manner as:

$$[M_2]\begin{bmatrix}\delta\dot{V}\\ \delta\dot{\phi}\end{bmatrix}=-[M_1]\begin{bmatrix}\delta V\\ \delta\phi\end{bmatrix} \tag{11}$$

The stability properties are determined by the eigenvalues of the following matrix:

$$[M_T]=-[M_2]^{-1}[M_1] \tag{12}$$

Note that we are describing the augmented oscillator with a reduced-order model, derived from (4). The number $M$ of eigenvalues agrees with the dimension of the differential-equation system resulting from the perturbation analysis. In this case, one has the system (10), so $M$ = 2. Since the matrix $[M_1]$ contains a column of zeroes, one of the two eigenvalues of $[M_T]$ is zero, $\lambda_1 = 0$, which is consistent with the autonomous behavior of the overall system. The second eigenvalue, $\lambda_2$, determines the stability properties of the loaded oscillator. For a stable behavior, one must have $\lambda_2 < 0$. This pole can be calculated analytically and is given by:

$$\lambda_2=-\frac{\frac{\partial Y_r}{\partial V}\left(\frac{\partial Y_i}{\partial\omega}+\frac{\partial Y_L{}^i(\omega)}{\partial\omega}\right)-\frac{\partial Y_i}{\partial V}\left(\frac{\partial Y_r}{\partial\omega}+\frac{\partial Y_L{}^r(\omega)}{\partial\omega}\right)}{\frac{1}{V_o^2}\left(\frac{\partial Y_r}{\partial\omega}+\frac{\partial Y_L{}^r(\omega)}{\partial\omega}\right)^2+\frac{1}{V_o^2}\left(\frac{\partial Y_i}{\partial\omega}+\frac{\partial Y_L{}^i(\omega)}{\partial\omega}\right)^2} \tag{13}$$

The pole $\lambda_2$ depends on the frequency derivative of the admittance of the slow-wave structure and will be equal to zero at the turning points of the solution curve. Thus, at the turning points there will be a qualitative change of stability since the real pole $\lambda_2$ crosses the imaginary axis.

Fig. 7(a) presents the variation of $\lambda_2$ through the solution curve in Fig. 5(a), using $L$ = 6 dB. At the turning points of the curve the condition $\lambda_2 = 0$ is satisfied. From the analysis in Fig. 7(a), the middle sections of the multi-valued intervals in Fig. 5(a) are unstable. The constant eigenvalues in standalone operation ($\lambda_{1o} = 0$ and $\lambda_{2o}$) are superimposed, for comparison. Fig. 7(b) presents the same analysis versus $V_{DS}$, for the case $W_2$ = 11.08 mm and $L$ = 8 dB, in Fig. 6(a), exhibiting a jump in the experimental trace. The lower section of the closed curve and the open curve are stable, whereas the upper section of the closed curve is unstable. This result is consistent with the experimental measurements.

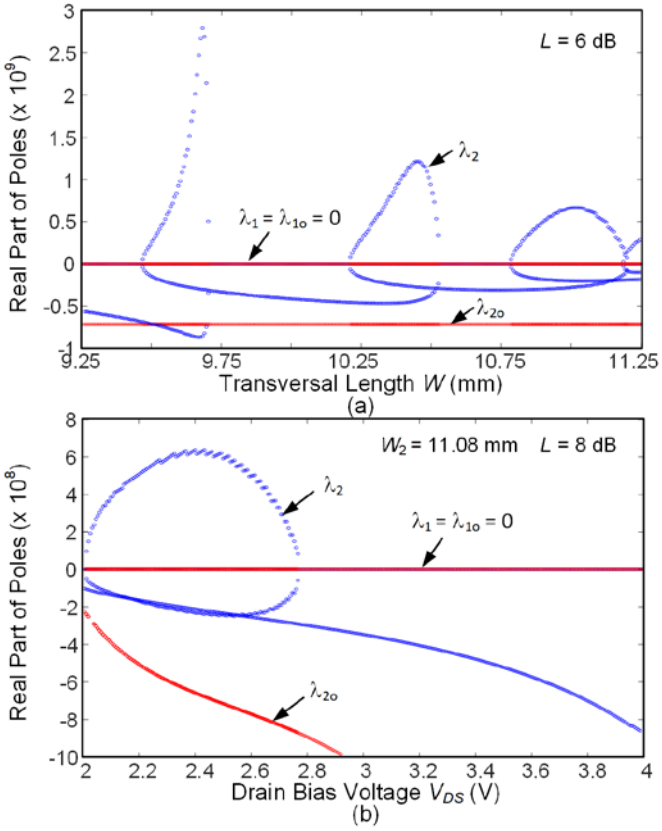


Fig. 7. Stability analysis. The eigenvalues of $[M_T]$ have been represented versus the analysis parameter. The constant poles ($\lambda_{1o} = 0$ and $\lambda_{2o}$), obtained under standalone operation are superimposed for comparison. (a) Versus the transversal length $W$. (b) Versus the drain bias voltage $V_{DS}$, for $W_2$ = 11.08 mm and $L$ = 8 dB.

### C. Noise analysis

For the noise analysis one equivalent noise source $I_N$ must be introduced at the connection node of the one-port network. Following the method in [19], its spectral density is fitted in a preliminary phase-noise analysis or measurement of the standalone oscillator. The equivalent noise source critically affects the matching between theory and measurements. However, this source is adjusted in standalone operation and kept at the fitted values when introducing the slow-wave structure. Thus, it cannot affect the phase-noise reduction. The equivalent noise source $I_N$ may account for both white and flicker noise, in a manner similar to the analysis in [29], where the flicker noise is represented as an additional low-frequency fluctuation of the perturbed system (at the fundamental frequency).

Introducing the noise source $I_N$ in system (11), applying the Fourier transform and solving for $\delta V, \delta\phi$, one obtains the following equation, in matrix form:

$$\begin{bmatrix} \delta V \\ \delta\phi \end{bmatrix} = \left[M_C(\Omega)\right] \begin{bmatrix} \dfrac{I_{Nr}}{V_o} \\ \dfrac{I_{Ni}}{V_o} \end{bmatrix} \tag{14}$$

where the subscripts $r$ and $i$ indicate real and imaginary part and $\Omega$ is the offset frequency and the matrix $[M_C]$ is:

$$\left[M_C(\Omega)\right] = \left\{ j\Omega \left[M_2\right] + \left[M_1\right] \right\}^{-1} \tag{15}$$

The noise spectral density is calculated from:

$$\begin{bmatrix} \delta V \\ \delta\phi \end{bmatrix} \left[\delta V \quad \delta\phi\right]^* = \left[M_C(\Omega)\right] \begin{bmatrix} \dfrac{\left\langle \left|I_N(\Omega)\right|^2 \right\rangle}{V_o^2} & 0 \\ 0 & \dfrac{\left\langle \left|I_N(\Omega)\right|^2 \right\rangle}{V_o^2} \end{bmatrix} \left[M_C(\Omega)\right]^+$$

$$= \left[M_C(\Omega)\right] \begin{bmatrix} \dfrac{2\left|I_w\right|^2 + k/\Omega}{V_o^2} & 0 \\ 0 & \dfrac{2\left|I_w\right|^2 + k/\Omega}{V_o^2} \end{bmatrix} \left[M_C(\Omega)\right]^+ \tag{16}$$

where the symbol "*" indicates conjugation and "+" indicates conjugate transpose. The spectral density $\left\langle \left|I_N(\Omega)\right|^2 \right\rangle$ of the equivalent noise-current source has been decomposed into white and flicker noise contributions and expressed as: $\left\langle \left|I_w\right|^2 \right\rangle = \left|I_w\right|^2 + k/\Omega$. Equation (16) is able to predict noise variations up to the order $\Omega^2$ in the numerator and the order $\Omega^4$ in the denominator. Solving for $\left\langle \left|\delta\phi\right|^2 \right\rangle$, the phase-noise spectral density is given by:

$$\left\langle \left|\delta\phi\right|^2 \right\rangle = \frac{\left( \left|\dfrac{\partial Y}{\partial V}\right|^2 + \left|\dfrac{\partial (Y+Y_L)}{\partial \omega}\right|^2 \dfrac{\Omega^2}{V_o^2} \right) \dfrac{2\left|I_w\right|^2 + k/\Omega}{V_o^2}}{\left( \det\left[J_o\right] + \dfrac{\partial Y_r}{\partial V}\dfrac{\partial Y_L{}^i}{\partial \omega} - \dfrac{\partial Y_i}{\partial V}\dfrac{\partial Y_L{}^r}{\partial \omega} \right)^2 \Omega^2 + \left|\dfrac{\partial (Y+Y_L)}{\partial \omega}\right|^4 \dfrac{\Omega^4}{V_o^2}} \tag{17}$$

where det() indicates determinant and the matrix $\left[J_o\right]$ is

$$\left[J_o\right] = \begin{bmatrix} \dfrac{\partial Y_r}{\partial V} & \dfrac{\partial Y_r}{\partial \omega} \\ \dfrac{\partial Y_i}{\partial V} & \dfrac{\partial Y_i}{\partial \omega} \end{bmatrix} \tag{18}$$

Note that the following term in the denominator of (17):

$$\det\left[J_o\right] + \frac{\partial Y_r}{\partial V}\frac{\partial Y_L{}^i}{\partial \omega} - \frac{\partial Y_i}{\partial V}\frac{\partial Y_L{}^r}{\partial \omega} = \frac{\partial Y_r}{\partial V}\left( \frac{\partial Y_i}{\partial \omega} + \frac{\partial Y_L{}^i(\omega)}{\partial \omega} \right) - \frac{\partial Y_i}{\partial V}\left( \frac{\partial Y_r}{\partial \omega} + \frac{\partial Y_L{}^r(\omega)}{\partial \omega} \right) \tag{19}$$

agrees with opposite of the numerator of the pole real $\lambda_2$. The coefficient (19) varies through the solution curve traced versus any parameter $\eta$. It will be zero at turning points of this curve and negative in the unstable sections. At the turning points, the phase noise does not tend to infinite due to the presence, in the denominator of (17), of the additional term in $\Omega^4$.

### D. Phase-noise reduction in FET-based oscillator

In the particular case of the transistor ATF34143, the dominant white noise source is a current source between the drain and source terminals, with the spectral density $\left\langle \left|I_d\right|^2 \right\rangle = 2.6\ 10^{-21}\ \mathrm{A^2/Hz}$ at $V_{GS} = 0$ V and $V_{DS} = 2.5$ V. The gate-to-source noise current source has the spectral density $\left\langle \left|I_g\right|^2 \right\rangle = 2.0\ 10^{-24}\ \mathrm{A^2/Hz}$ and the cross-correlation noise between the two sources is in the order of $< I_g I_d^* >= j1.46\ 10^{-23}\ \mathrm{A^2/Hz}$. On the other hand, the flicker noise current is usually modeled, as in this case, with a current noise source, connected between the intrinsic drain and source terminals. Taking the data provided by the manufacturer as initial values, the equivalent current source $\left\langle |\, I_N\, |^2 \right\rangle$ was fitted to match the measured phase-noise spectral density of the standalone oscillator [32]. Note that the flicker-noise contribution The resulting values for the white-noise source and up-converted flicker noise were $\left|I_w\right|^2 = 0.25\ 10^{-20}\ \mathrm{A^2/Hz}$, $k = 1.91\ 10^{-14}\ \mathrm{A^2/Hz}$. The simulated and measured spectra are compared in Fig. 2(c). Fig. 8(a) presents the phase-noise variation though the solution curve versus $W$ in Fig. 5(a), at the constant offset frequency 100 kHz. Fig. 8(b) compares this phase-noise variation with that of the coefficient affecting $\Omega^2$ in the denominator of (17). This comparison is discussed in Subsection *E*. The spectral density of the free-running oscillator at the same offset frequency is superimposed, for comparison. At the experimental point indicated in the figure, a phase-noise reduction of 13 dB is achieved.

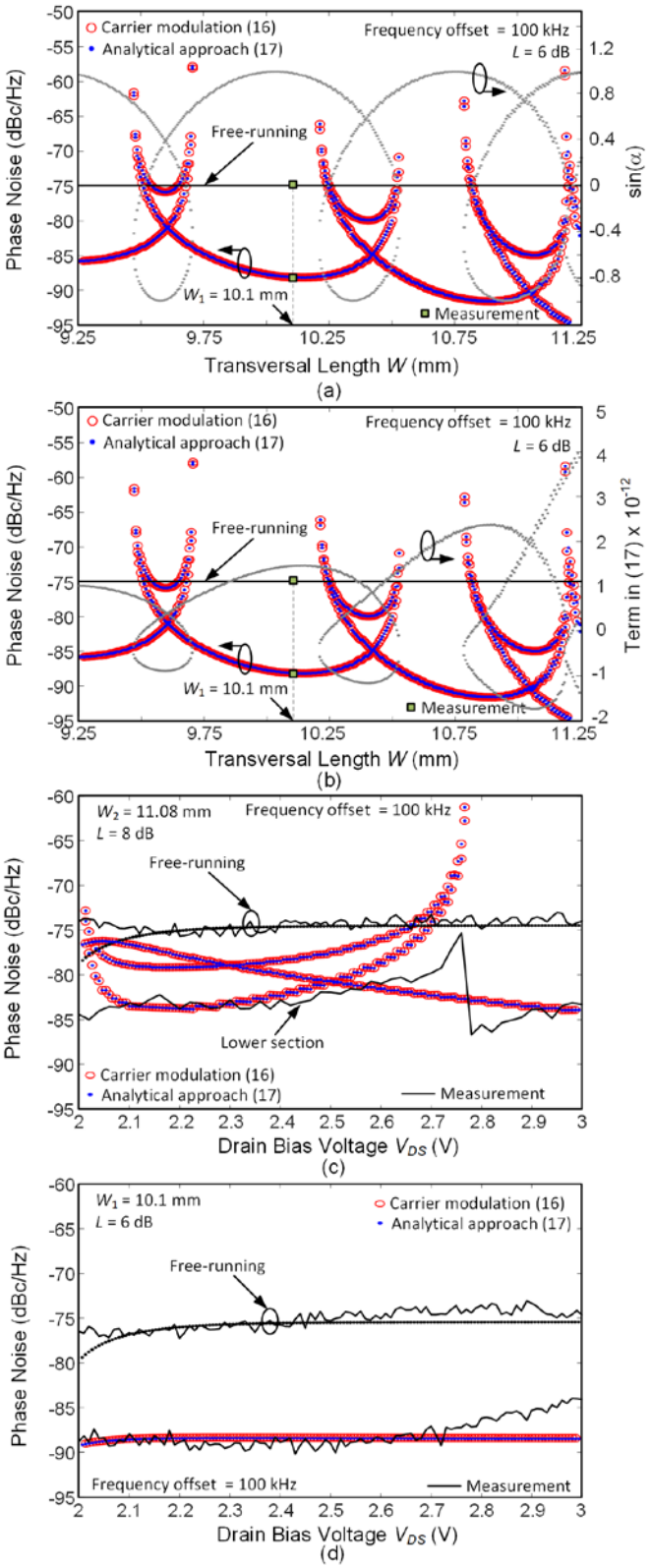


Fig. 8. Variation of the phase-noise spectral density at the constant offset frequency 100 kHz. (a) Versus $W$. Comparison with the variation of the angle $\alpha$ in (25). (b) Versus $W$. Comparison with the variation of the coefficient affecting $\Omega^2$ in the denominator of (17). (c) Versus $V_{DS}$, for $W_2$ = 11.08 mm and $L$ = 8 dB. (d) Versus $V_{DS}$, for $W_1$ = 10.1 mm and $L$ = 6 dB.

Fig. 8(c) and Fig. 8(d) present the variation of the phase-noise spectral density at 100 kHz versus $V_{DS}$ for the two cases considered in Fig. 6. The results are validated with experimental traces obtained with the R&S® FSWP8 analyzer. For $W_2$ = 11.08 mm and $L$ = 8 dB, in Fig. 6(a), the stable lower section of the closed curve shows a maximum phase-noise reduction [Fig. 8(c)] of about 8 dB with respect to the free-running value. The phase-noise spectral density calculated through (17) exhibits a high value at the turning point *TP*, different from infinite, due to the presence of the $\Omega^4$ term in the denominator. Through the open curve, after the turning point, the phase-noise reduction with respect to the free-running value is about 10 dB. The expression (17) and its relationship with the real pole (13) explains the experimental observations in Fig. 8(c). For $W_1$ = 10.1 mm and $L$ = 6 dB, in Fig. 6(b), there are no jumps and the phase-noise reduction is about 13 dB [Fig. 8(d)].

Fig. 9 presents a comparison of the phase-noise spectrum obtained for $W_1$ = 10.1 mm, $L$ = 6 dB and $V_{DS}$ = 2.5 V with the one obtained in free-running conditions for the same $V_{DS}$ value. The optimum spectrum attained with the topology based on the circulator is also superimposed, for comparison.

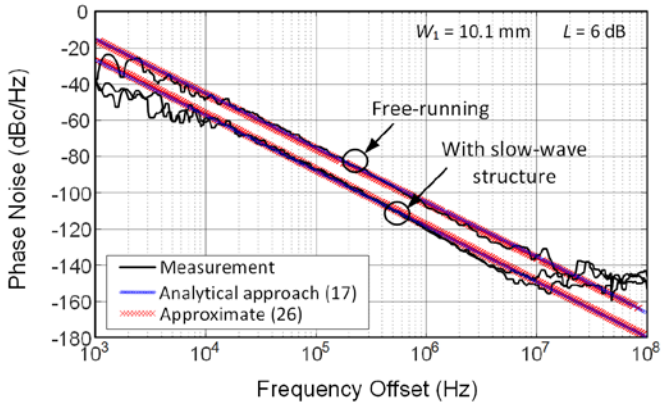


Fig. 9. Comparison of the phase-noise spectrum resulting for $W_1$ = 10.1 mm, $L$ = 6 dB and $V_{DS}$ = 2.5 V with the one obtained in free-running conditions for the same $V_{DS}$. The optimum spectrum obtained with the topology based on the circulator is also superimposed. The spectra obtained with the complete expression (17) and with the approximation (26) are nearly overlapped.

### *E. Mechanism for the phase-noise reduction*

To get insight into the mechanism for phase-noise reduction, some simplifications may be carried out. Up to a certain frequency offset $\Omega_y$ it is possible to neglect the term in $\Omega^2$ (affecting the noise source) in the numerator of (17). This offset frequency is calculated by making equal the magnitudes of the two terms in the numerator, which provides:

$$\Omega_y = \frac{|Y_V|V_o}{\left|\frac{\partial(Y+Y_L)}{\partial\omega}\right|} \tag{20}$$

where $Y_V$ is the amplitude derivative of the admittance function. Note that because the order of magnitude of the frequency derivatives is smaller than that of the amplitude derivative, $\Omega_y$ will be generally rather large. For instance, at the operation point indicated in Fig. 8(a), corresponding to $W_1$ = 10.1 mm and $L$ = 6 dB, this offset frequency is $f_y$ = 71.7 MHz. On the other hand, the two terms in $\Omega^2$ and $\Omega^4$ in the denominator become equal at the following corner frequency:

$$\Omega_{3\mathrm{dB}}=\frac{\left|\det\left[J_o\right]+\dfrac{\partial Y_r}{\partial V}\dfrac{\partial Y_L{}^i}{\partial\omega}-\dfrac{\partial Y_i}{\partial V}\dfrac{\partial Y_L{}^r}{\partial\omega}\right|}{\left|\dfrac{\partial(Y+Y_L)}{\partial\omega}\right|^2}V_o \tag{21}$$

Comparing the above expression with the one in (13) for the eigenvalue $\lambda_2$, one will have $\Omega_{3\mathrm{dB}}=0$ when $\lambda_2=0$, which occurs at the turning points of the solution curve. At these points, only the term in $\Omega^4$ remains in the denominator of (17). However, unless operating near a turning point, the corner frequency $\Omega_{3\mathrm{dB}}$ will also have a large value. For $W_1$ = 10.1 mm and $L$ = 6 dB, this corner frequency is $f_y$ = 71.27 MHz. Thus, for $\Omega << \Omega_y$ and $\Omega << \Omega_{3\mathrm{dB}}$, equation (17) can be approximated as:

$$\left\langle\left|\delta\phi\right|^2\right\rangle=\frac{1}{\Omega^2}\frac{\left|\dfrac{\partial Y}{\partial V}\right|^2\dfrac{2\left|I_w\right|^2+k/\Omega}{V_o^2}}{\left(\det\left[J_o\right]+\dfrac{\partial Y_r}{\partial V}\dfrac{\partial Y_L{}^i}{\partial\omega}-\dfrac{\partial Y_i}{\partial V}\dfrac{\partial Y_L{}^r}{\partial\omega}\right)^2} \tag{22}$$

This phase-noise spectrum can be compared with that of the standalone oscillator:

$$\left\langle\left|\delta\phi_o\right|^2\right\rangle=\frac{1}{\Omega^2}\frac{\left|\dfrac{\partial Y}{\partial V}\right|^2\dfrac{2\left|I_w\right|^2+k/\Omega}{V_o^2}}{\left(\det\left[J_o\right]\right)^2} \tag{23}$$

So the phase-noise reduction is:

$$\frac{\left\langle\left|\delta\phi\right|^2\right\rangle}{\left\langle\left|\delta\phi_o\right|^2\right\rangle}=\frac{\left(\det\left[J_o\right]\right)^2}{\left(\det\left[J_o\right]+\dfrac{\partial Y_r}{\partial V}\dfrac{\partial Y_L{}^i}{\partial\omega}-\dfrac{\partial Y_i}{\partial V}\dfrac{\partial Y_L{}^r}{\partial\omega}\right)^2} \tag{24}$$

As gathered from (24), the reduction should be approximately independent of the offset frequency, in full agreement with the spectrum of Fig. 9. The denominator of (24) can be expressed as:

$$\left(\det\left[J_o\right]+\left|\frac{\partial Y}{\partial V}\right|\left|\frac{\partial Y_L(\omega)}{\partial\omega}\right|\sin\alpha(\omega)\right)^2 \tag{25}$$

where $\alpha(\omega)$ is the angle between the frequency derivative and the amplitude derivative. To illustrate the impact of $\alpha(\omega)$, the function $\sin(\alpha)$ has been superimposed in Fig. 8(a). As can be seen, it varies between -1 and 1. The highest positive values are obtained in the parameter intervals providing the greatest phase-noise reductions. The function $\sin(\alpha)$ takes a zero value at the parameter values at which the phase-noise agrees with that of the standalone oscillator circuit. It takes negative values within the multivalued sections. At the turning points of the solution curve, the phase-noise increases sharply.

At the points with maximum phase-noise reduction $\sin(\alpha)$ is not exactly 1 because the magnitude $\left|\partial Y_L(\omega)/\partial\omega\right|$ also has an effect on the phase-noise reduction, as gathered from the expressions (24) and (25). This can be seen in Fig. 8(b), where the term $\left|\partial Y/\partial V\right|\left|\partial Y_L(\omega)/\partial\omega\right|\sin\alpha(\omega)$ has been traced versus $W$. The local maxima of phase-noise reduction are obtained at the local maxima of this term.

To have an estimation of the maximum achievable phase-noise reduction for a given group delay $\tau_g(\omega)$, one can approximate $\sin(\alpha)\cong 1$ and $Y_L(\omega)\cong -2\rho(\omega)Y_o e^{j\phi(\omega)}$, due to the high attenuation values. Then, the phase-noise spectral density can be expressed as:

$$\left\langle\left|\delta\phi\right|^2\right\rangle\cong\frac{\left|\dfrac{\partial Y}{\partial V}\right|^2\dfrac{2\left|I_w\right|^2+k/\Omega}{V_o^2}}{\Omega^2\left[\det\left[J_o\right]+\left|\dfrac{\partial Y}{\partial V}\right|2\rho(\omega)Y_o\tau_g(\omega)\right]^2} \tag{26}$$

where $\tau_g(\omega)=-\partial\phi(\omega)/\partial\omega$ and the frequency derivative $\partial\rho(\omega)/\partial\omega$ has been neglected. This is because the term contributed by $\partial\rho(\omega)/\partial\omega$ to the derivative $\partial Y_L(\omega)/\partial\omega$ is several orders of magnitude smaller than the one contributed by $\partial\phi(\omega)/\partial\omega$. For instance, at 2.73 GHz the first term is $3.33\cdot10^{-13}+j9.744\cdot10^{-13}\ \Omega^{-1}/\mathrm{s}^{-1}$ and the second term is $-4.01\cdot10^{-10}+j1.37\cdot10^{-10}\ \Omega^{-1}/\mathrm{s}^{-1}$. From (26), the maximum reduction of the phase-noise spectral density is larger for a higher group delay $\tau_g(\omega)$. Note that expression (26) is only valid near the maxima of phase-noise reduction. It has been applied for $W_1$ = 10.1 mm and $L$ = 6 dB and the results are superimposed in Fig. 9.

Qualitatively, the phase-noise reduction is due to the increase in the oscillator quality factor when this oscillator is loaded with the slow-wave structure. Using a commonly employed definition for the oscillator quality factor $Q$ [30], the maximum $Q$ value of the augmented oscillator is:

$$Q=\frac{\omega_o}{2Y_o}\frac{\partial[Y^i+Y_L^i(\omega_o)]}{\partial\omega}=Q_o+\frac{\omega_o}{Y_o}\rho(\omega_o)Y_o\tau_g(\omega_o) \tag{27}$$

where $Q_o$ is the quality factor of the standalone oscillator.

As shown in the flowchart of Fig. 2, the optimization procedure consists of three steps (i) Initial optimization of the slow-wave structure, which must be suitably chosen to obtain a high group delay $\tau_g(\omega)$ at the desired oscillation frequency $\omega_o$, as done in Fig. 4. (ii) Verification of the stable operation of the augmented oscillator in a single-valued section of the solution curve. Note that instabilities when dealing with high Q elements have been reported in previous works [5], [17]. (iii) Fine tuning of the parameters in the slow-wave structure to maximize the phase noise reduction at the desired oscillation frequency.

## III. Two-port Configuration

In the two-port configuration (Fig. 10), the slow-wave structure is connected between the output and input of the oscillator circuit. A small portion of the output signal passes through the slow-wave structure, which stabilizes this signal, due to the long delay. In comparison with the one-port configuration, the transistor gain may enable a higher phase-noise reduction. However, the trade-off regarding circuit stability must be investigated, as done in the following.

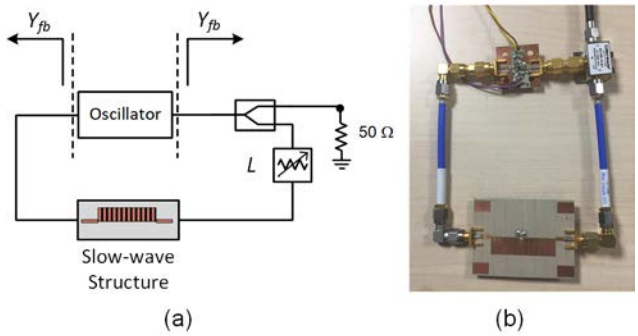


Fig. 10. Oscillator system including a two-port feedback network containing the SS-OS slow-wave structure. (a) Schematic. (b) Photograph.

### *A. Steady-state solutions*

The steady-state analysis of the oscillator with a two-port feedback network requires the extraction a two-port model of the standalone oscillator. This oscillator will be described in terms of two admittance functions, $Y_1$ and $Y_2$, calculated at the two nodes where the feedback network will be connected (Fig. 11). In free-running conditions, these two admittance functions are simultaneously equal to zero.

$$\begin{aligned} Y_1(V_{1o}, V_{2o}, \phi_o, \omega_o) &= 0 \\ Y_2(V_{1o}, V_{2o}, \phi_o, \omega_o) &= 0 \end{aligned} \tag{28}$$

where $\omega_o$ is the free-running oscillation frequency, $V_{1o}$ and $V_{2o}$, are the steady-state amplitudes at the two nodes, 1 and 2, (between which the feedback network will be connected) and $\phi_o$ is the phase shift between these two voltages.

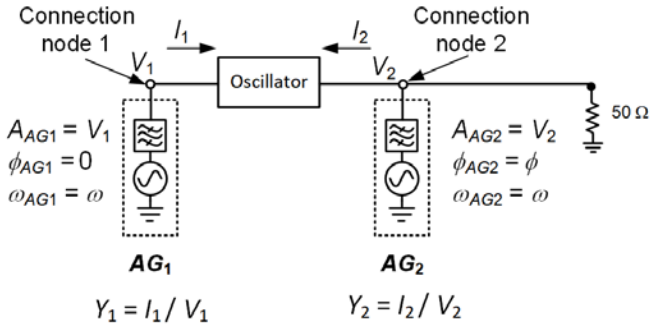


Fig. 11. Sketch of the procedure to obtain the derivatives of the two outer-tier admittance functions that constitute the numerical oscillator model.

The feedback network is described in terms of its two-port admittance matrix $[Y_{fb}]$. In case this network replaces any terminal elements of the standalone oscillator circuit, the admittance matrix used for the oscillator analysis must take into account this replacement. For instance, in the case of Fig. 11, one should consider the difference $[Y_L] = [Y_{fb}]-[Y_o]$, where $[Y_o]$ is 2×2 matrix with $Y_{o,ij} = 0$ except $Y_{o,22} = Y_o$. Because the feedback network should not significantly alter the oscillatory solution, it must be possible to expand the admittance functions in a first-order Taylor series about the free-running solution of the standalone oscillator. This provides the following system.

$$\begin{aligned} &\frac{\partial Y_1}{\partial V_1}V_{1o}\Delta V_1 + \frac{\partial Y_1}{\partial V_2}V_{1o}\Delta V_2 + \frac{\partial Y_1}{\partial \phi}V_{1o}\Delta\phi + \\ &\frac{\partial Y_1}{\partial \omega}V_{1o}(\omega-\omega_o) + Y_{11}(\omega)V_{1o} + Y_{12}(\omega)V_{2o}e^{j\phi_o} = 0 \\ &\frac{\partial Y_2}{\partial V_1}V_{2o}e^{j\phi_o}\Delta V_1 + \frac{\partial Y_2}{\partial V_2}V_{2o}e^{j\phi_o}\Delta V_2 + \\ &\frac{\partial Y_2}{\partial \phi}V_{2o}e^{j\phi_o}\Delta\phi + \frac{\partial Y_2}{\partial \omega}V_{2o}e^{j\phi_o}(\omega-\omega_o) + \\ &Y_{21}(\omega)V_{1o} + Y_{22}(\omega)V_{2o}e^{j\phi_o} = 0 \end{aligned} \tag{29}$$

where $Y_{ij}$ are the parameters of the matrix $[Y_L]$, $\Delta V_1 = V_1 - V_{1o}$, $\Delta V_2 = V_2 - V_{2o}$ and $\Delta\phi = \phi - \phi_o$. On the other hand, the derivatives are calculated introducing two AGs in the standalone oscillator, at the connection nodes of the feedback network. At the quiescent point, the two AGs values correspond to those of the free-running oscillation, calculated with a suitable number (NH) of harmonic terms. They operate at the frequency $\omega_o$, with amplitudes, $V_{1o}$ and $V_{2o}$. The phase of the first AG is arbitrarily set to zero and the phase $\phi_o$ of the second AG is set to the difference between the phase values of the two node voltages. Then, finite differences are applied to the two AGs, in terms of the four variables $V_1$, $V_2$, $\phi$ and $\omega$, performing a HB analysis for each variable increment and calculating the resulting increments in the two AG admittance functions. The same number NH of harmonic terms is considered for this finite-difference calculation.

For a simpler analysis of (29), the constant exponential $e^{j\phi_o}$ will be absorbed in various terms of this equation system:

$$\begin{aligned} &Y_{12}'(\omega) = Y_{12}(\omega)e^{j\phi_o}, \quad \frac{\partial Y_2'}{\partial V_1} = \frac{\partial Y_2}{\partial V_1}e^{j\phi_o} \\ &\frac{\partial Y_2'}{\partial V_2} = \frac{\partial Y_2}{\partial V_2}e^{j\phi_o}, \quad \frac{\partial Y_2'}{\partial \phi} = \frac{\partial Y_2}{\partial \phi}e^{j\phi_o} \\ &\frac{\partial Y_2'}{\partial \omega} = \frac{\partial Y_2}{\partial \omega}e^{j\phi_o}, \quad Y_{22}'(\omega) = Y_{22}(\omega)e^{j\phi_o} \end{aligned} \tag{30}$$

For compactness, the following functions will also be introduced:

$$\begin{aligned} H_1(\omega) &= -\left[Y_{11}(\omega) + Y_{12}'(\omega)\gamma\right] \\ H_2(\omega) &= -\left[Y_{21}(\omega)\beta + Y_{22}'(\omega)\right] \end{aligned} \tag{31}$$

where $\gamma = \frac{V_{2o}}{V_{1o}}$, $\beta = \frac{V_{1o}}{V_{2o}}$. Due to the circuit gain $\gamma >> \beta$. For instance, in the oscillator considered here, $\gamma = 7.02$ and $\beta = 0.142$. For the sake of accuracy and generality, all the terms will be considered in the following derivations. However, insightful simplifications will be carried out once the final accurate expressions have been derived. Splitting (29) into real and imaginary parts one obtains:

$$\begin{aligned}
&\frac{\partial Y_{1,r}}{\partial V_1}\Delta V_1+\frac{\partial Y_{1,r}}{\partial V_2}\Delta V_2+\frac{\partial Y_{1,r}}{\partial \phi}\Delta\phi+\frac{\partial Y_{1,r}}{\partial \omega}(\omega-\omega_o)=H_{1,r}(\omega)\\
&\frac{\partial Y_{1,i}}{\partial V_1}\Delta V_1+\frac{\partial Y_{1,i}}{\partial V_2}\Delta V_2+\frac{\partial Y_{1,i}}{\partial \phi}\Delta\phi+\frac{\partial Y_{1,i}}{\partial \omega}(\omega-\omega_o)=H_{1,i}(\omega)\\
&\frac{\partial Y'_{2,r}}{\partial V_1}\Delta V_1+\frac{\partial Y'_{2,r}}{\partial V_2}\Delta V_2+\frac{\partial Y'_{2,r}}{\partial \phi}\Delta\phi+\frac{\partial Y'_{2,r}}{\partial \omega}(\omega-\omega_o)=H_{2,r}(\omega)\\
&\frac{\partial Y'_{2,i}}{\partial V_1}\Delta V_1+\frac{\partial Y'_{2,i}}{\partial V_2}\Delta V_2+\frac{\partial Y'_{2,i}}{\partial \phi}\Delta\phi+\frac{\partial Y'_{2,i}}{\partial \omega}(\omega-\omega_o)=H_{2,i}(\omega)
\end{aligned} \tag{32}$$

where the subscripts *r* and *i* indicate real and imaginary parts. System (32) can be written in a compact matrix form as:

$$[J_o]\Delta\bar{X}=\bar{H} \tag{33}$$

where

$$\begin{aligned}
\Delta\bar{X}&=\left[\Delta V_1 \quad \Delta V_2 \quad \Delta\phi \quad (\omega-\omega_o)\right]^T\\
\bar{H}&=\left[H_{1,r}(\omega) \quad H_{1,i}(\omega) \quad H_{2,r}(\omega) \quad H_{2,i}(\omega)\right]^T
\end{aligned} \tag{34}$$

And $[J_o]$ is the Jacobian matrix of the oscillator core, given by:

$$[J_o]=\begin{bmatrix}
\frac{\partial Y_{1,r}}{\partial V_1} & \frac{\partial Y_{1,r}}{\partial V_2} & \frac{\partial Y_{1,r}}{\partial \phi} & \frac{\partial Y_{1,r}}{\partial \omega}\\
\frac{\partial Y_{1,i}}{\partial V_1} & \frac{\partial Y_{1,i}}{\partial V_2} & \frac{\partial Y_{1,i}}{\partial \phi} & \frac{\partial Y_{1,i}}{\partial \omega}\\
\frac{\partial Y'_{2,r}}{\partial V_1} & \frac{\partial Y'_{2,r}}{\partial V_2} & \frac{\partial Y'_{2,r}}{\partial \phi} & \frac{\partial Y'_{2,r}}{\partial \omega}\\
\frac{\partial Y'_{2,i}}{\partial V_1} & \frac{\partial Y'_{2,i}}{\partial V_2} & \frac{\partial Y'_{2,i}}{\partial \phi} & \frac{\partial Y'_{2,i}}{\partial \omega}
\end{bmatrix} \tag{35}$$

Note that (35) only depends on the original oscillator design. It is independent of the slow-wave structure. Then, the steady-state solutions can be directly obtained by calculating the zeroes of the error function:

$$\begin{aligned}
&E(\omega)=(\omega-\omega_o)+A_{1o}H_{1,r}(\omega)-\\
&A_{2o}H_{1,i}(\omega)+A_{3o}H_{2,r}(\omega)-A_{4o}H_{2,i}(\omega)=0
\end{aligned} \tag{36}$$

where the following constant terms have been introduced:

$$\begin{aligned}
A_{1o}&=\frac{cofact\left(\frac{\partial Y_{1,r}}{\partial \omega}\right)}{\det(J_o)},\ A_{2o}=-\frac{cofact\left(\frac{\partial Y_{1,i}}{\partial \omega}\right)}{\det(J_o)}\\
A_{3o}&=\frac{cofact\left(\frac{\partial Y'_{2,r}}{\partial \omega}\right)}{\det(J_o)},\ A_{4o}=-\frac{cofact\left(\frac{\partial Y'_{2,i}}{\partial \omega}\right)}{\det(J_o)}
\end{aligned} \tag{37}$$

As in the case of the one-port slow-wave structure, the solution curves (in terms of the oscillation frequency $\omega$ versus any parameter $\eta$ of the slow-wave structure, such as the transversal length *W*) can be traced by plotting the zero-value contour of the function *E*. This will be done by simulating the slow-wave structure only. A double sweep is performed in the particular slow-wave parameter, for instance $\eta = W$, and the excitation frequency $\omega$. This gives rise to a double dependence of $[Y_L]$ on $\eta$ and $\omega$. Once the double entry admittance matrix $\left[Y_{fb}(\eta,\omega)\right]$ is available, one can trace the contour $E(\eta,\omega)=0$ in the plane defined by $\eta$ and $\omega$. The expression for the contour is:

$$\begin{aligned}
&E(\eta,\omega)=(\omega-\omega_o)+A_{1o}H_{1,r}(\eta,\omega)-\\
&A_{2o}H_{1,i}(\eta,\omega)+A_{3o}H_{2,r}(\eta,\omega)-A_{4o}H_{2,i}(\eta,\omega)=0
\end{aligned} \tag{38}$$

Once the oscillation frequency is known, the rest of variables, $\Delta V_1, \Delta V_2, \Delta\phi$, can be calculated in a straightforward manner, by solving them from system (32).

The above procedure has been applied to the oscillator in Fig. 3(a) and 3(b). The slow-wave structure, acting as a feedback network, is connected between the output and input ports of the oscillator circuit. As already stated, the input port is defined between the terminal *T* and ground, where a connector has been introduced [Fig. 3(b)]. Fig. 12(a) presents the variations of the oscillation frequency $\omega$ versus the transversal length *W* of the SS-OS slow-wave structure, with the attenuation *L* = 16 dB. Note that larger *L* values are needed due to the higher sensitivity at the device input port. The contour $E(W,\omega)=0$ is compared with the curve obtained through a numerical solution of the same error equation. We would like to emphasize that the equations considered in the two cases are identical. Therefore, the same results are expected, even if in Fig. 12(a) a slight difference emerges, close to the turning points, between the two solution methods.

In Fig. 12(a), we also compare the results with those obtained through a HB simulation with 15 harmonic terms, unable to pass by default through the turning points. As expected the most noticeable discrepancies with HB are obtained at the larger frequency excursions, where the accuracy of the Taylor series expansion degrades. The range of variation of the oscillation frequency is much larger than in the one-port case, due to the higher sensitivity at the transistor input port. It could be reduced with a higher attenuation but this would also limit the phase-noise reduction capabilities. Fortunately, the quasi-oscillatory response of the augmented oscillator allows setting the oscillation frequency to the original free-running value. Fig. 12(b) presents the variation versus *W* of the oscillation amplitudes at the two ports between which the feedback network is connected. The curve obtained with the analytical formulation can also be compared with circuit-level HB simulations of the augmented oscillator. The discontinuities in the HB trace are indicative of bad convergence properties. This convergence completely fails in the multi-valued sections, which cannot be predicted with HB. Measurement points are superimposed, which have been obtained using an Agilent 1134A differential probe. At 2.73 GHz, the amplitude ratio varies from $\gamma_o = 7.02$ in free-running conditions to $\gamma = 6.234$. The discrepancy in amplitude can only be attributed to inaccuracies in the models of the circuit components.

In the analysis of Fig. 12(c), the transversal length *W* is kept constant and the attenuation *L* is varied. The oscillation frequency $\omega$ has been traced versus *L* for two values of the transversal length, marked in Fig. 12(a): $W_1 = 8.8$ mm, providing an oscillation frequency equal to the free-running one, $f = f_o = 2.73$ GHz, and $W_2 = 8$ mm, within a multi-valued

section. Note the consistency between this solution curve versus $L$ and the one in Fig. 12(a), versus $W$.

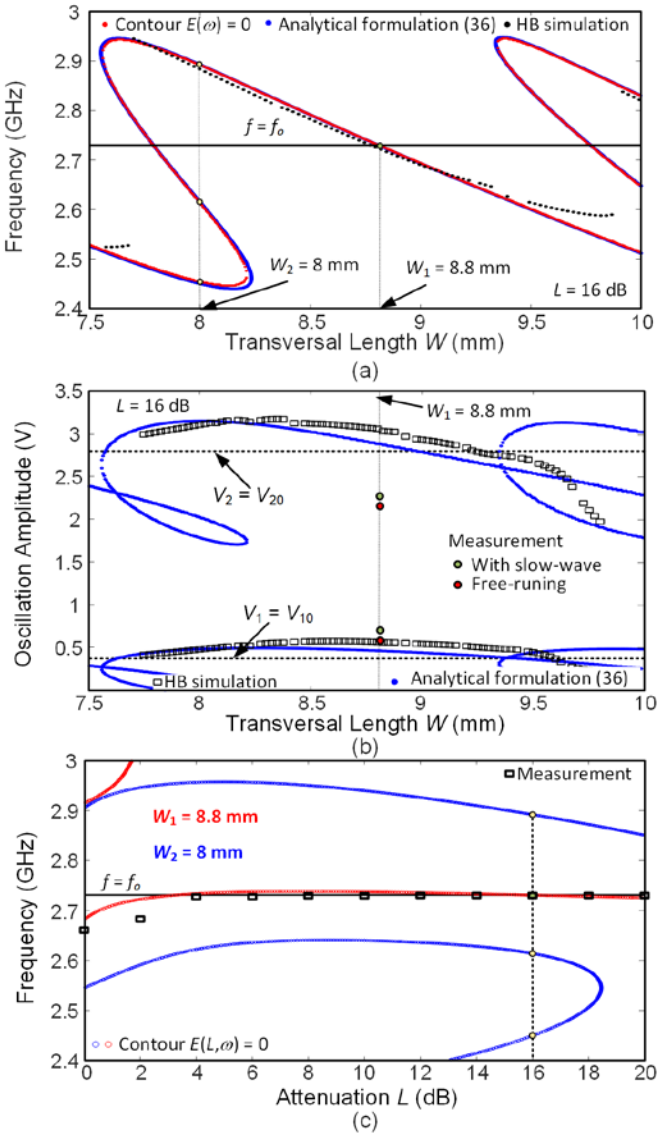


Fig. 12. Feedback with a two-port network containing the SS-OS slow-wave structure. (a) Oscillation frequency $\omega$ versus the transversal length $W$ for the attenuation $L$ = 16 dB. Results are compared with those obtained through a numerical solution of (38) and through HB with NH = 15. (b) Variation of the voltage amplitudes at the input and output ports of the augmented oscillator versus $W$ for $L$ = 16 dB. Results are compared with HB simulations. (c) Oscillation frequency $\omega$ versus $L$ for two values of the transversal length, marked in (a): $W_1$ = 8.8 mm and $W_2$ = 8 mm.

### *B. Stability analysis*

Applying a small perturbation to system (32), the node-voltage amplitudes and phases become $V_1+\delta V_1(t)$, $V_2+\delta V_2(t)$, $0+\delta\phi_1(t)$, $\phi_o+\delta\phi_2(t)$ and the frequency becomes $\omega - js$ [28]-[29]. Taking also into account that $s$ acts as a time differentiator, one obtains:

$$\frac{\partial Y_1}{\partial V_1}\delta V_1+\frac{\partial Y_1}{\partial V_2}\delta V_2-\left(\frac{\partial Y_1}{\partial \phi}+jY_{12}^{'}(\omega)\gamma\right)\delta\phi_1+\left(\frac{\partial Y_1}{\partial \phi}+jY_{12}^{'}(\omega)\gamma\right)\delta\phi_2+\left(\frac{\partial Y_1}{\partial \omega}+\frac{\partial Y_{11}(\omega)}{\partial \omega}\right)\left(-j\frac{\delta\dot{V}_1}{V_{1o}}+\delta\dot{\phi}_1\right)+\frac{\partial Y_{12}^{'}(\omega)}{\partial \omega}\gamma\left(-j\frac{\delta\dot{V}_2}{V_{2o}}+\delta\dot{\phi}_2\right)=0$$

$$\frac{\partial Y_2}{\partial V_1}\delta V_1+\frac{\partial Y_2}{\partial V_2}\delta V_2+\left(-\frac{\partial Y_2}{\partial \phi}+jY_{21}^{'}(\omega)\beta\right)\delta\phi_1+\left(\frac{\partial Y_2}{\partial \phi}-jY_{21}^{'}(\omega)\beta\right)\delta\phi_2+\left(\frac{\partial Y_{21}^{'}(\omega)}{\partial \omega}\beta\right)\left(-j\frac{\delta\dot{V}_1}{V_{1o}}+\delta\dot{\phi}_1\right)+\left(\frac{\partial Y_2}{\partial \omega}+\frac{\partial Y_{22}(\omega)}{\partial \omega}\right)\left(-j\frac{\delta\dot{V}_2}{V_{2o}}+\delta\dot{\phi}_2\right)=0 \quad (39)$$

where the following definition has been used:

$$Y_{21}^{'}(\omega)=Y_{21}(\omega)e^{-j\phi_o} \quad (40)$$

Splitting (39) into real and imaginary parts, one obtains the following system in matrix form:

$$[M_2]\delta\dot{\bar{X}}=-[M_1]\delta\bar{X} \quad (41)$$

where $\delta\bar{X}=[\delta V_1(t)\quad \delta V_2(t)\quad \delta\phi_1(t)\quad \delta\phi_2(t)]^T$. Each of the two matrixes $[M_1]$ and $[M_2]$ can be decomposed into one matrix accounting for the core oscillator (indicated with the subscript "*o*") and a matrix accounting for the feedback network (indicated with subscript "*fb*"), as shown in the following:

$$\left\{[M_{2o}]+[M_{2fb}]\right\}\delta\dot{\bar{X}}=-\left\{[M_{1o}]+[M_{1fb}]\right\}\delta\bar{X} \quad (42)$$

And the matrixes are given by:

$$[M_{1o}]=\begin{bmatrix}\frac{\partial Y_{1,r}}{\partial V_1} & \frac{\partial Y_{1,r}}{\partial V_2} & -\frac{\partial Y_{1,r}}{\partial \phi} & \frac{\partial Y_{1,r}}{\partial \phi}\\ \frac{\partial Y_{1,i}}{\partial V_1} & \frac{\partial Y_{1,i}}{\partial V_2} & -\frac{\partial Y_{1,i}}{\partial \phi} & \frac{\partial Y_{1,i}}{\partial \phi}\\ \frac{\partial Y_{2,r}}{\partial V_1} & \frac{\partial Y_{2,r}}{\partial V_2} & -\frac{\partial Y_{2,r}}{\partial \phi} & \frac{\partial Y_{2,r}}{\partial \phi}\\ \frac{\partial Y_{2,i}}{\partial V_1} & \frac{\partial Y_{2,i}}{\partial V_2} & -\frac{\partial Y_{2,i}}{\partial \phi} & \frac{\partial Y_{2,i}}{\partial \phi}\end{bmatrix} \quad (43)$$

$$[M_{1fb}]=\begin{bmatrix}0 & 0 & Y_{12,i}^{'}(\omega)\gamma & -Y_{12,i}^{'}(\omega)\gamma\\ 0 & 0 & -Y_{12,r}^{'}(\omega)\gamma & Y_{12,r}^{'}(\omega)\gamma\\ 0 & 0 & -Y_{21,i}^{'}(\omega)\beta & Y_{21,i}^{'}(\omega)\beta\\ 0 & 0 & Y_{21,r}^{'}(\omega)\beta & -Y_{21,r}^{'}(\omega)\beta\end{bmatrix} \quad (44)$$

$$[M_{2o}]=\begin{bmatrix} \frac{\partial Y_{1,i}}{\partial\omega}\frac{1}{V_{1o}} & 0 & \frac{\partial Y_{1,r}}{\partial\omega} & 0 \\ -\frac{\partial Y_{1,r}}{\partial\omega}\frac{1}{V_{1o}} & 0 & \frac{\partial Y_{1,i}}{\partial\omega} & 0 \\ 0 & \frac{\partial Y_{2,i}}{\partial\omega}\frac{1}{V_{2o}} & 0 & \frac{\partial Y_{2,r}}{\partial\omega} \\ 0 & -\frac{\partial Y_{2,r}}{\partial\omega}\frac{1}{V_{2o}} & 0 & \frac{\partial Y_{2,i}}{\partial\omega} \end{bmatrix} \quad (45)$$

$$[M_{2fb}]=\begin{bmatrix} \frac{\partial Y_{11,i}}{\partial\omega}\frac{1}{V_{1o}} & \frac{\partial Y'_{12,i}(\omega)}{\partial\omega}\frac{\gamma}{V_{2o}} & \frac{\partial Y_{11,r}}{\partial\omega} & \frac{\partial Y'_{12,r}(\omega)}{\partial\omega}\gamma \\ -\frac{\partial Y_{11,r}}{\partial\omega}\frac{1}{V_{1o}} & -\frac{\partial Y'_{12,r}(\omega)}{\partial\omega}\frac{\gamma}{V_{2o}} & \frac{\partial Y_{11,i}}{\partial\omega} & \frac{\partial Y'_{12,i}(\omega)}{\partial\omega}\gamma \\ \frac{\partial Y'_{21,i}(\omega)}{\partial\omega}\frac{\beta}{V_{1o}} & \frac{\partial Y_{22,i}}{\partial\omega}\frac{1}{V_{2o}} & \frac{\partial Y'_{21,r}(\omega)}{\partial\omega}\beta & \frac{\partial Y_{22,i}}{\partial\omega} \\ -\frac{\partial Y'_{21,r}(\omega)}{\partial\omega}\beta & -\frac{\partial Y_{22,r}}{\partial\omega} & \frac{\partial Y'_{21,i}(\omega)}{\partial\omega}\beta & \frac{\partial Y_{22,i}}{\partial\omega} \end{bmatrix} \quad (46)$$

The stability properties are determined by the four eigenvalues of the matrix $[M_T]=[M_2]^{-1}[M_1]$. Note that both the one-port and two-port analyses constitute reduced-order descriptions of the augmented oscillator, which lead to differential equation systems with different dimensions. The two-port analysis is based on a two (complex) admittance functions, so the order of the derived differential-equation system $M = 4$. Thus, one obtains 4 eigenvalues. One of these eigenvalues is zero, due to the autonomous behavior of the whole system (in the presence of the feedback loop). This zero eigenvalue is consistent with the singularity of $[M_1]$ and the fact that the whole oscillator system is invariant with respect to any arbitrary phase shift $\Delta\phi$, equally applied to the two node voltages, by doing $0+\Delta\phi$, $\phi_o+\Delta\phi$.

The results of the stability analysis are presented in Fig. 13. In Fig. 13(a), the real part of the four eigenvalues is traced versus $W$. The constant poles corresponding to the standalone oscillator are also superimposed for comparison. One of these poles is $\lambda_{1o} = 0$. There is also a real pole, $\lambda_{2o}$, and a pair of complex-conjugate poles, $\lambda_{3o}$ and $\lambda_{4o}$. For experimental-validation purposes, the analysis has also been carried out in terms of the oscillator drain-bias voltage, $V_{DS}$, with the results shown in Fig. 13(b). The circuit is stable for the whole range of $V_{DS}$ values. This stable behavior will be confirmed with the phase-noise measurements of the next section.

### C. Noise analysis

The phase noise analysis of an oscillator including a two-port feedback network can be carried out considering, in principle, two equivalent noise sources $I_{N1}$ and $I_{N2}$, introduced in parallel at the connection nodes of the feedback network. These sources must be included in the perturbation system (39), which gives rise to an additional vector $\bar{I}_N$ on the right side of this equation. Applying the Fourier transform, the noisy system is written as:

$$\delta\bar{X}=[M_C(\Omega)]\begin{bmatrix} I_{N1r}/V_{1o} \\ I_{N1i}/V_{1o} \\ I_{N2r}/V_{2o} \\ I_{N2i}/V_{2o} \end{bmatrix} \quad (47)$$

where $V_{1o}$ and $V_{2o}$ are the voltage amplitudes in free-running conditions and $[M_C(\Omega)]$ is:

$$[M_C(\Omega)]=\{j\Omega\,[M_2]+[M_1]\}^{-1} \quad (48)$$

Then, the circuit noise is calculated multiplying $\delta\bar{X}$ in (47) by the conjugate transpose $\delta\bar{X}^+$. All the noise terms, including the cross correlation ones, are directly obtained from the matrix $\delta\bar{X}\,\delta\bar{X}^+$. In particular, the phase noise at the two connection nodes of the feedback network is given by $\left\langle|\delta\phi_m|^2\right\rangle$, where $m$ = 1,2.

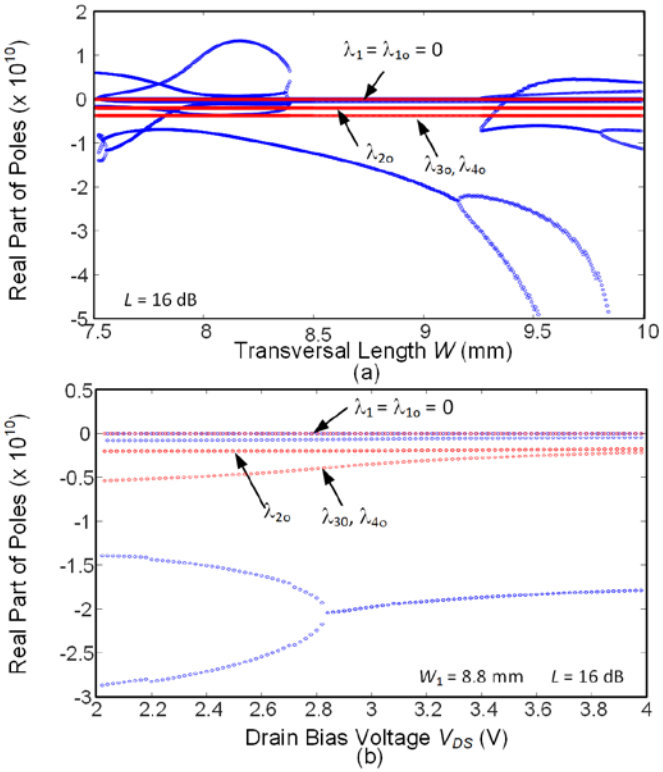


Fig. 13. Stability analysis of the oscillator in Fig. 10 under the effect of a two-port feedback network, containing the SS-OS structure. The real part of the poles has been represented versus the analysis parameter. The constant poles obtained under standalone operation are superimposed for comparison. (a) Versus the transversal length $W$. (b) Versus the drain bias voltage $V_{DS}$.

To get some insight into the mechanism for the phase-noise reduction, an alternative formulation, based on the calculation of the modulation of the oscillation frequency, $\delta\omega$, will also be derived. This formulation is conceptually equivalent to the carrier-modulation approach [25], [28]. It takes into account that the steady-state solution of a free-running oscillator is invariant versus constant phase shifts. In fact, to solve the oscillator-equation system, one sets the phase of one state variable to zero and replaces it with the unknown oscillation frequency. In the carrier-modulation approach, the phase of the state variable is kept at zero even in the presence of noise sources. Though more approximate than the method based on

(48), the calculation of the frequency modulation is simpler, so, in the case of the oscillator augmented with the slow-wave structure, it enables a better insight into the mechanism for phase-noise reduction.

In our formulation, the phase shift of node 1, given by $\delta\phi_1$, is replaced with $\delta\omega$. In the presence of noise perturbations, one obtains the following system:

$$\begin{bmatrix} \frac{\partial Y_{1,r}}{\partial V_1} & \frac{\partial Y_{1,r}}{\partial V_2} & \frac{\partial Y_{1,r}}{\partial \phi} & \left(\frac{\partial Y_{1,r}}{\partial \omega}-\frac{\partial H_{1,r}(\omega)}{\partial \omega}\right) \\ \frac{\partial Y_{1,i}}{\partial V_1} & \frac{\partial Y_{1,i}}{\partial V_2} & \frac{\partial Y_{1,i}}{\partial \phi} & \left(\frac{\partial Y_{1,i}}{\partial \omega}-\frac{\partial H_{1,i}(\omega)}{\partial \omega}\right) \\ \frac{\partial Y'_{2,r}}{\partial V_1} & \frac{\partial Y'_{2,r}}{\partial V_2} & \frac{\partial Y'_{2,r}}{\partial \phi} & \left(\frac{\partial Y'_{2,r}}{\partial \omega}-\frac{\partial H_{2,r}(\omega)}{\partial \omega}\right) \\ \frac{\partial Y'_{2,i}}{\partial V_1} & \frac{\partial Y'_{2,i}}{\partial V_2} & \frac{\partial Y'_{2,i}}{\partial \phi} & \left(\frac{\partial Y'_{2,i}}{\partial \omega}-\frac{\partial H_{2,i}(\omega)}{\partial \omega}\right) \end{bmatrix} \begin{bmatrix} \delta V_1 \\ \delta V_2 \\ \delta\phi \\ \delta\omega \end{bmatrix} = \begin{bmatrix} \frac{I_{N1,r}}{V_{1o}} \\ \frac{I_{N1,i}}{V_{1o}} \\ \frac{I_{N2,r}}{V_{2o}} \\ \frac{I_{N2,i}}{V_{2o}} \end{bmatrix} \tag{49}$$

Solving for $\delta\omega$ one obtains:

$$\delta\omega = \frac{-A_{1o}I_{N1r}/V_{1o} + A_{2o}I_{N1i}/V_{1o} - A_{3o}I_{N2r}/V_{2o} + A_{4o}I_{N2i}/V_{2o}}{\det[J_o] + H_\omega(\omega)} \tag{50}$$

where $A_{mo}$, with $m$ = 1 to 4, had been defined in (37), and only depend on the steady-state solution of the original oscillator (without the slow-wave structure) and the following quantity has been introduced:

$$H_\omega(\omega) = -\frac{\partial H_{1,r}}{\partial \omega}A_{1o} - \frac{\partial H_{1,i}}{\partial \omega}A_{2o} - \frac{\partial H_{2,r}}{\partial \omega}A_{3o} - \frac{\partial H_{2,i}}{\partial \omega}A_{4o} \tag{51}$$

Taking into account that $\delta\omega = j\Omega\delta\phi$, and considering that the two noise sources are uncorrelated, the phase-noise spectral density is given by:

$$\left\langle |\delta\phi|^2 \right\rangle = \frac{\left( (A_{1o}^2 + A_{2o}^2)\frac{\left\langle |I_{N1}|^2 \right\rangle}{V_{1o}^2} + (A_{3o}^2 + A_{4o}^2)\frac{\left\langle |I_{N2}|^2 \right\rangle}{V_{2o}^2} + (A_{1o}A_{3o} + A_{2o}A_{4o})\frac{\mathrm{Re}\left\langle I_{N1}I_{N2}^* \right\rangle}{V_{1o}V_{2o}} + (A_{1o}A_{4o} - A_{2o}A_{3o})\frac{\mathrm{Im}\left\langle I_{N1}I_{N2}^* \right\rangle}{V_{1o}V_{2o}} \right)}{\Omega^2\left(\det[J_o] + H_\omega(\omega)\right)^2} \tag{52}$$

In the absence of the two-port feedback, the denominator of (52) is $\Omega^2\left(\det[J_o]\right)^2$, so the phase-noise reduction is due to $H_\omega(\omega)$. However, due to the circuit gain from input to output, not all the terms in (51) will have the same impact. Taking into account the definitions in (31) and the fact that $\gamma >> \beta$, one can write:

$$\begin{aligned} H_\omega(\omega) &\cong \gamma\left(\frac{\partial Y'_{12,r}(\omega)}{\partial\omega}A_{1o} + \frac{\partial Y'_{12,i}(\omega)}{\partial\omega}A_{2o}\right) \\ &= \gamma\left|\frac{\partial Y'_{12}(\omega)}{\partial\omega}\right|\left|A_{12,o}\right|\cos\theta(\omega) \end{aligned} \tag{53}$$

where $A_{12,o} = A_{1o} + jA_{2o}$ and $\theta$ is the angle between the two complex numbers, which will vary with the parameters of the slow-wave structure. Note that that $A_{12,o}$ depends on the steady-state solution of the standalone oscillator only. As in the case of the one-port network, the maximum phase-noise reduction will increase with the group delay, as this increases the magnitude of the frequency derivative $\partial Y'_{12}/\partial\omega$. There will also be minima and maxima, due to the sinusoidal dependence.

To calculate the phase-noise spectral density we have considered the input and output noise current sources, as well as their correlation term, which, in this particular case, has negligible effect. Fig. 14(a) presents the variation of the phase-noise spectral density at the constant frequency offset 100 kHz versus the transversal length *W*. The phase-noise spectral density of the free-running oscillator at the same offset frequency is superimposed, for comparison. The results of (47) and (52) exhibit some discrepancies in the multi-valued intervals. This is because only the method derived from (47) is able to predict resonance effects due to near critical poles in the offset-frequency range of the oscillator spectrum.

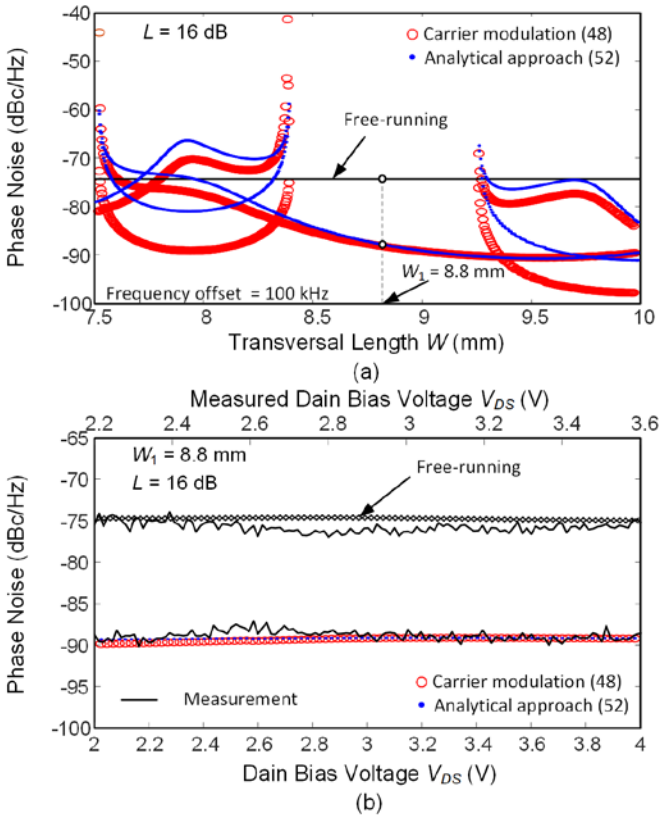


Fig. 14. Oscillator using a feedback configuration containing the SS-OS slow-wave structure. Variation of the phase-noise spectral density at the constant offset frequency 100 kHz. (a) Versus transversal length *W*. (b) For *W* = 8.8mm

versus the drain bias voltage $V_{DS}$. Results obtained in simulation and measurements are compared.

Fig. 14(b) presents the variation of the phase-noise spectral density obtained for $W$ = 8.8 mm, at 100 kHz, versus the drain bias voltage $V_{DS}$, obtained in simulation and measurement. As can be seen, the oscillator is stable for the whole $V_{DS}$ range, in agreement with the predictions of Fig. 13(b). In both simulation and measurement, the spectral density exhibits very small variations. The spectral density corresponding to the free-running oscillator at the same offset frequency is superimposed, for comparison. The phase-noise reduction with respect to free-running operation is about 15 dB.

An additional test with the slow-wave structure in Fig. 1(d), with the attenuation $L$ = 16 dB, has been carried out. Fig. 15 presents the variation of the phase-noise spectral density at 100 kHz versus the drain bias voltage $V_{DS}$, obtained in simulation and measurement. As in the previous case, the system is stable in the whole $V_{DS}$ range. For $V_{DS}$ = 2 V, a phase-noise reduction of 18 dB is achieved. Finally, Fig. 16 presents a comparison of the phase-noise spectrum, at $V_{DS}$ = 2 V, with the one obtained in free-running conditions for the same $V_{DS}$ value.

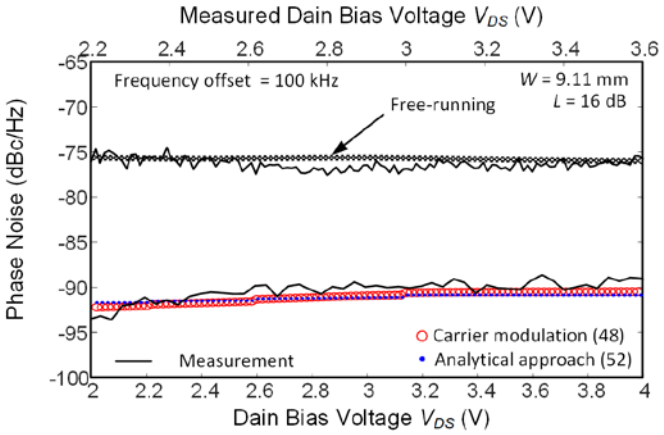


Fig. 15. Phase noise when using a feedback network containing the slow-wave in Fig. 1(d). Variation of the phase-noise spectral density at 100 kHz versus $V_{DS}$, obtained in simulation and measurement.

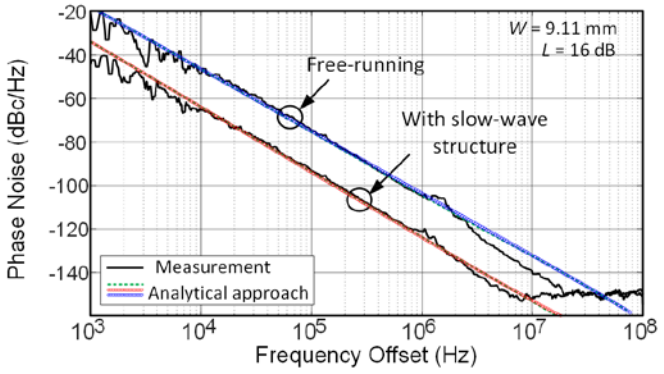


Fig. 16. Phase noise spectrum when using the slow-wave structure in Fig. 1(d), with the attenuation $L$ = 16 dB. The drain bias voltage is $V_{DS}$ = 2 V.

## IV. Conclusions

A methodology to reduce the phase-noise spectral density of an existing oscillator through the connection of an external network, containing a slow-wave structure, has been presented. One problem associated with the long delay is the appearance of multi-valued solutions when considering variations in a relevant parameter, such as a length or width. These complex solution curves can be efficiently predicted with an analytical equation that combines a numerical oscillator model, extracted from harmonic-balance simulations, with the results of a linear analysis of the slow-wave structure. The corresponding error function can be introduced in the data display of the linear analysis software, so the solution curve agrees with the zero-error contour in terms of the excitation/oscillation frequency and the analysis parameter. Several ways to connect the slow-wave structure have been proposed and compared. Its introduction as a two-port feedback network requires the extraction of an outer-tier model of the standalone oscillator circuit based on two admittance functions. A perturbation analysis enables the determination of the stability properties and the phase-noise spectral density. The various analysis and design methodologies have been applied to an oscillator operating at 2.73 GHz. A phase-noise reduction of 13 dB has been achieved with an external one-port network and a reduction of 18 dB has been achieved with an external two-port network.

## References

[1] B. Razavi, “Study of phase noise in CMOS oscillators”, *IEEE J. Solid State Circuits*, vol. 31, pp. 331–343, 1996.

[2] U. L. Rohde, A. K. Poddar, G. Böck, *The Design of Modern Microwave Oscillators for Wireless Applications: Theory and Optimization*, New York: John Wiley & Sons, 2005.

[3] U. L. Rohde, *Microwave and Wireless Synthesizers: Theory and Design*, Wiley-Interscience, New York, 1997.

[4] H.-C. Chang, "Stability analysis of self-injection-locked oscillators," *IEEE Trans. Microw. Theory Techn.*, vol. 51, no. 9, pp. 1989-1993, Sept. 2003.

[5] H.-C. Chang, "Phase noise in self-injection-locked oscillators - theory and experiment," *IEEE Trans. Microw. Theory Techn.*, vol. 51, no. 9, pp. 1994-1999, Sept. 2003.

[6] A. Suárez, F. Ramírez, “Analysis of Stabilization Circuits for Phase-Noise Reduction in Microwave Oscillators,” *IEEE Trans. Microw. Theory Techn.*, vol. 53, no. 9, pp. 2743 –2751, Sep. 2005.

[7] K. Peng, C. Lee, D. Wong, F. Wang and T. Horng, "An Injection- and Frequency-Locked Loop for Reducing Phase Noise of Wideband Oscillators," *IEEE Trans. Microw. Theory Techn.*, vol. 66, no. 3, pp. 1374-1383, March 2018.

[8] Y.-C. Huang and S.-I. Liu, “A 2.4 GHz sub-harmonically injection locked PLL with self-calibrated injection timing,” in *ISSCC Dig.*, Feb. 2012, pp. 338–340

[9] J. M. Avila-Ruiz, L. Moreno-Pozas, E. Duran-Valdeiglesias, A. Moscoso-Martir, I. Molina-Fernandez and J. de-Oliva-Rubio, "Frequency locked loop architecture for phase noise reduction in wideband low-noise microwave oscillators," in *IET Microwaves, Antennas & Propagation*, vol. 7, no. 11, pp. 869-875, 20 August 2013.

[10] J. M. Ávila-Ruiz, I. Molina-Fernández, L. Moreno-Pozas and A. Moscoso-Mártir, "Ultra-Wideband VCO Phase-Noise Reduction Loop Based on a Six-Port Phase-Shifterless Delay-Line Discriminator," *IEEE Trans. Microw. Theory Techn.*, vol. 62, no. 12, pp. 3076-3084, Dec. 2014.

[11] M. Pontón, F. Ramírez, A. Herrera, A. Suárez, “Phase-Noise Reduction in Self-Injection Locked Oscillators Using Slow-Wave Structures,” *IEEE MTT-S Int. Microw. Symp. Dig.*, Boston, MA, 2019, pp. 1-4.

[12] C. Zhou, H. Y. D. Yang, "Design Considerations of Miniaturized Least Dispersive Periodic Slow-Wave Structures," *IEEE Trans. Microw. Theory Techn.*, vol. 56, no. 2, pp. 467-474, Feb. 2008.

[13] J. Selga, P. Vélez, J. Bonache and F. Martín, “High miniaturization potential of slow-wave transmission lines based on simultaneous inductor

and capacitor loading," 2017 47th *European Microw. Conf.* (EuMC), Nuremberg, 2017, pp. 783-386.
[14] W.S. Chang, C.Y. Chang, "A high slow-wave factor microstrip structure with simple design formulas and its application to microwave circuit design," *IEEE Trans. Microw. Theory Techn.*, vol. 60, no. 11, pp. 3376 – 3383, Nov. 2012.
[15] A. K. Poddar, U. L. Rohde, "Slow Wave Resonator based tunable oscillators," *IEEE Int. Frequency Control and Europ. Frequency and Time Forum (FCS) Proc.*, San Francisco, CA, USA, 2011, pp. 1-10.
[16] A. K. Poddar, U. L. Rohde, "Slow-Wave Evanescent-Mode coupled resonator oscillator ciruits," *IEEE Int. Frequency Control Symp. Proc.*, Baltimore, MD, 2012, pp. 1-7.
[17] J. C. Nallatamby, M. Prigent, M. Camiade, J. Obregon, Phase-nise in oscillators-Leeson formula revisited, *IEEE Trans. Microw. Theory Techn.*, vol. 51, no. 4, pp. 1032-1046, Apr. 2003.
[18] F. Ramirez, M. E. de Cos and A. Suarez, "Nonlinear analysis tools for the optimized design of harmonic-injection dividers," *IEEE Trans. Microw. Theory Techn.*, vol. 51, no. 6, pp. 1752-1762, June 2003.
[19] F. Ramírez, M. Pontón, S. Sancho, A. Suárez, "Phase−Noise Analysis of Injection−Locked Oscillators and Analog Frequency Dividers", *IEEE Trans. Microw. Theory Techn.*, vol. 56, no.2, pp. 393−407, 2008.
[20] A. Suarez, F. Ramirez and S. Sancho, "Stability and Noise Analysis of Coupled-Oscillator Systems," *IEEE Trans. Microw. Theory Techn.*, vol. 59, no. 4, pp. 1032-1046, Apr. 2011.
[21] F. Ramírez, S. Sancho, M. Pontón and A. Suárez, "Two-Scale Envelope-Domain Analysis of Injected Chirped Oscillators," *IEEE Trans. Microw. Theory Techn.*, vol. 66, no. 12, pp. 5449-5461, Dec. 2018.
[22] L. O. Chua, "A switching-parameter algorithm for finding multiple solutions of nonlinear resistive circuits", *Int. J. Circuit Theory and Appl.*, vol. 4, no. 3, July 1976.
[23] H. G. Brachtendorf, R. Melville, P. Feldmann, S. Lampe and R. Laur, "Homotopy Method for Finding the Steady States of Oscillators," *IEEE Trans. Comput.-Aided Design Int. Circuits and Systems*, vol. 33, no. 6, pp. 867-878, June 2014.
[24] B. Schiffman, "A new class of broad-band microwave 90-degree phase shifters," *IRE Trans. Microw. Theory Techn.*, vol. 6, no. 2, pp. 232 –237, Apr. 1958.
[25] V. Rizzoli, F. Mastri, and D. Masotti, "General noise analysis of nonlinear microwave circuits by the piecewise harmonic-balance technique," *IEEE Trans. Microw. Theory Techn.*, vol. 42, no. 5, pp. 807–819, May 1994.
[26] A. Suárez, R. Quéré, *Stability Analysis of Nonlinear Microwave Circuits*. Boston, MA: Artech House, 2003.
[27] A. Suárez, *Analysis and Design of Autonomous Microwave Circuits*. Hoboken, NJ: Wiley IEEE Pres, 2009.
[28] K. Kurokawa, "Some basic characteristics of broadband negative resistance oscillators", *Bell Syst. Tech. J.*, vol. 48, pp. 1937–1955, July–Aug. 1969.
[29] K. Kurokawa, "Noise in Synchronized Oscillators," *IEEE Trans. Microw. Theory Techn.*, vol. 16, no. 4, pp. 234-240, April 1968.
[30] P. F. Combes, J. Graffeuil, J-F. Sautereau, *Microwave Components, Devices, and Active Circuits*, John Wiley & Sons, Chichester, Sussex, England, 1987.
[31] N. B. Buchanan and V. Fusco, "Single VCO chipless RFID near-field reader," *Elect. Lett.*, vol. 52, no. 23, pp. 1958-1960, 11 10 2016.
[32] M. Odyniec (editor), "RF and Microwave Oscillator Design", Artech House, Norwood, MA, USA, 2002.

**Mabel Pontón** (S'08–M'11) was born in Santander, Spain. She received the bachelor's degree in Telecommunication Engineering, master's degree in Information Technologies and Wireless Communications Systems, and Ph.D. degree from the University of Cantabria, Santander, in 2004, 2008, and 2010, respectively. In 2006, she joined the Communications Engineering Department, University of Cantabria.

From 2011 to 2013, she was with the Group of Electronic Design and Applications, Georgia Institute of Technology, Atlanta, GA, USA, as a Post-Doctoral Research Fellow.

Her current research interests include the nonlinear analysis and simulation of radiofrequency and microwave circuits, with an emphasis on phase-noise, stability, and bifurcation analysis of complex oscillator topologies.

**Franco Ramírez** (S'03-A'05-M'05-SM'16) obtained a degree in electronic systems engineering degree from the Military School of Engineering (EMI) in La Paz, Bolivia, in 2000 and the Ph.D. degree in Communications Engineering from the University of Cantabria, Santander, Spain in 2005. From 1999 to 2000, he worked for Ericsson de Bolivia Telecomunicaciones, where he was involved in projects related with GSM and TDMA technologies. From 2009 to 2005, Dr. Ramírez was a Research Fellow of the "Ramón y Cajal" Programme, funded by the Spanish Ministry of Science and Innovation, at the Communications Engineering Department of the University of Cantabria, where he is currently an Associate Professor. His research interests include phase noise, stability and the development of nonlinear techniques for the analysis and design of autonomous microwave circuits.

**Amparo Herrera** was born in Asturias (Spain) in 1963. She received the degree in Electronic Physics from the University of Cantabria (Spain) in June 1987, and the Ph.D degree from the same University in June 1995. In 1987 she joined the CIDA (Centro de Investigación y Desarrollo de la Armada) the Research and Development Spanish Army Centre, working on developing a RF&Microwave laboratory up to 1990 when she joined the Electronics Department of the University of Cantabria, working on MMIC design. From 1992 to 1995, she collaborated with the Laboratory Philips Microwave Limeil (actually OMMIC), as result of this collaboration she presents her thesis receiving the Ph.D. degree in Electronics from the University of Cantabria in June 1995 in this work she had designed a high efficiency power amplifier for DECT and DCS applications a work for the Philips Microwave Limeill foundry (now called OMMIC). From 1995 she has been an associate professor at the University of Cantabria, and a member of its Communications Engineering Department. Her areas of interest include the MMIC and Hybrid design of microwave circuits and, specially, the power and low noise amplifier design and characterization. She has taken part as Main researcher in a big number of Spanish and European projects both of the III, IV, V and VI Frameworks and Spanish National R&D Plan. Also she has participated in a number of industrial projects with European and Spanish industries. Currently she is working in the design and development of MMIC devices on Si-Ge, GaN PHEMT technologies.

**Almudena Suárez** (M'96–SM'01–F'12) was born in Santander, Spain. She received the Electronic Physics and Ph.D. degrees from the University of Cantabria, Santander, Spain, in 1987 and 1992, respectively, and the Ph.D. degree in Electronics from the University of Limoges, Limoges, France, in 1993.

She is currently a Full Professor with the Communications Engineering Department, University of Cantabria. She co-authored *Stability Analysis of Nonlinear Microwave Circuits* (Artech House, 2003) and authored *Analysis and Design of Autonomous Microwave Circuits* (IEEE-Wiley, 2009).

Prof. Suárez is a member of the Technical Committees of the IEEE Microwave Theory and Techniques Society (IEEE MTT-S) International Microwave Symposium (IMS) and the European Microwave Conference. She was an IEEE Distinguished Microwave Lecturer from 2006 to 2008. She is a member of the Board of Directors of the European Microwave Association. She was the Coordinator of the Communications and Electronic Technology Area for the Spanish National Evaluation and Foresight Agency between 2009 and 2013. In 2014 and 2015 she was the co-chair of IEEE Topical Conference on RF Power Amplifiers (PAWR). Prof. Suárez is the Editor-in-Chief of the International Journal of Microwave and Wireless Technologies from Cambridge University Press journals and an Associate Editor for IEEE Microwave Magazine.